JGR Solid Earth

RESEARCH ARTICLE
10.1029/2022JB024885

Key Points:

- An isotropic and anisotropic surface wave dispersion database across Alaska is constructed for Rayleigh and Love waves from 8 to 85 s
- Three-station direct-wave interferometry greatly improves the number and quality of measurements compared to two-station interferometry
- The Rayleigh wave azimuthally anisotropic pattern beneath the Alaska-Aleutian subduction zone reflects the effect of the subducting slab

Supporting Information:

Supporting Information may be found in the online version of this article.

Correspondence to:

C. Liu,
chuanming.liu@colorado.edu

Citation:

Liu, C., Zhang, S., Sheehan, A. F., & Ritzwoller, M. H. (2022). Surface wave isotropic and azimuthally anisotropic dispersion across Alaska and the Alaska-Aleutian subduction zone. *Journal of Geophysical Research: Solid Earth*, *127*, e2022JB024885. https://doi.org/10.1029/2022JB024885

Received 13 JUN 2022
Accepted 25 OCT 2022

Author Contributions:

Conceptualization: Chuanming Liu, Anne F. Sheehan, Michael H. Ritzwoller
Data curation: Chuanming Liu
Formal analysis: Chuanming Liu
Funding acquisition: Anne F. Sheehan, Michael H. Ritzwoller
Investigation: Chuanming Liu
Methodology: Chuanming Liu, Shane Zhang, Michael H. Ritzwoller
Project Administration: Michael H. Ritzwoller
Software: Chuanming Liu, Shane Zhang
Supervision: Michael H. Ritzwoller
Validation: Chuanming Liu
Visualization: Chuanming Liu, Shane Zhang
Writing – original draft: Chuanming Liu

Surface Wave Isotropic and Azimuthally Anisotropic Dispersion Across Alaska and the Alaska-Aleutian Subduction Zone

Chuanming Liu[1], Shane Zhang[1], Anne F. Sheehan[2], and Michael H. Ritzwoller[1]

[1]Department of Physics, University of Colorado Boulder, Boulder, CO, USA, [2]Department of Geological Sciences, Cooperative Institute for Research in Environmental Sciences, University of Colorado Boulder, Boulder, CO, USA

Abstract Comprehensive observations of surface wave anisotropy across Alaska and the Aleutian subduction zone are needed to improve understanding of its tectonics, mantle dynamics, and earthquake risk. We produce such observations, using stations from the USArray Transportable Array and regional networks across Alaska and the Alaska Amphibious Community Seismic Experiment in the Alaska-Aleutian subduction zone both onshore and offshore. Our data include Rayleigh and Love wave phase dispersion from earthquakes (28–85 s) and ambient noise two- and three-station interferometry (8–50 s). Compared with using two-station interferometry alone, three-station interferometry significantly improves the signal-to-noise ratio and approximately doubles the number of measurements retained. Average differences between both isotropic and anisotropic tomographic maps constructed from different methods lie within their uncertainties, which is justification for combining the measurements. The composite tomographic maps include Rayleigh wave isotropy and azimuthal anisotropy from 8 to 85 s both onshore and offshore, and onshore Love wave isotropy from 8 to 80 s. In the Alaska-Aleutian subduction zone, Rayleigh wave fast directions vary from trench parallel to perpendicular and back to parallel with increasing periods, apparently reflecting the effect of the subducted Pacific Plate. The tomographic maps provide a basis for inferring the 3-D anisotropic crustal and uppermost mantle structure across Alaska and the Aleutian subduction zone.

Plain Language Summary We construct a new database across continental Alaska and the Alaska-Aleutian subduction zone of directionally dependent measurements of the speed of seismic surface waves. The application of a new method in which observations at three stations at a time are considered improves the number and quality of measurements. Our results resolve the local directional-dependence of seismic wave speeds (anisotropy) and in many cases, are directly related to known geological structures in the earth's crust and upper mantle. The complicated anisotropy beneath the Alaska-Aleutian subduction zone reflects the complex tectonic environment in this region. This study provides the basis for constructing a 3D seismic model of anisotropy beneath Alaska and the subduction zone.

1. Introduction

The North American plate in Alaska is an amalgamation of many tectonic terranes (e.g., Colpron et al., 2007) (Figure 1a). The present terranes result from multiple long-term episodes of accretion, accumulation, and deformation due to the dynamic and complex plate boundary interactions of the Pacific, Siberian, and North American Plates (e.g., Shephard et al., 2013). Northern Alaska is a passive margin and was accreted in the late Jurassic (e.g., Moore & Box, 2016; Till, 2016). The Alaskan Interior experienced complex collisional and extensional deformation in the Permian and Cretaceous periods (e.g., Johnston, 2001; Plafker & Berg, 1994). In southern Alaska, accreted terranes docked in the late Mesozoic to Cenozoic, and strike-slip zones developed due to the subduction of the Pacific Plate and Yakutat microplate (e.g., Shephard et al., 2013). Offshore southern Alaska, the Alaska-Aleutian subduction zone is one of the most tectonically and seismically active convergent margins in the world. Historically, a series of great earthquakes have occurred along the megathrust boundary (Figure 1a).

With the recent deployment of the USArray Transportable Array (TA) in continental Alaska (Busby & Aderhold, 2020) and the Alaska Amphibious Community Seismic Experiment (AACSE) in the Alaska Peninsula and offshore (Barcheck et al., 2020), as well as other regional networks, new seismic data have become available to investigate the tectonic architecture and history of deformation of Alaska and the subduction zone both onshore and offshore (Figure 1b). Previous seismic studies in Alaska have focused both on the isotropic and anisotropic structure of the crust and mantle. Isotropic seismic models have been presented based on seismic reflection and

Writing – review & editing: Chuanming Liu, Shane Zhang, Anne F. Sheehan, Michael H. Ritzwoller

refraction profiling (e.g., Fuis et al., 2008; Li et al., 2015; Shillington et al., 2015), receiver functions (e.g., Miller & Moresi, 2018; Zhang et al., 2019), surface wave tomography (e.g., Feng, 2021; Feng & Ritzwoller, 2019; Mann et al., 2021; Wang & Tape, 2014; Yang & Gao, 2020), body waves (e.g., Eberhart-Phillips et al., 2006; Gou et al., 2019), joint surface wave and receiver function tomography (e.g., Berg et al., 2020; Gama et al., 2021; Martin-Short et al., 2018; Ward & Lin, 2018), and joint surface wave and body wave tomography (e.g., Jiang et al., 2018; Nayak et al., 2020). Crustal and mantle azimuthally anisotropy has been primarily investigated using local shear-wave splitting (e.g., Richards et al., 2021), teleseismic shear-wave splitting (e.g., Lynner, 2021; McPherson et al., 2020; Venereau et al., 2019), surface wave tomography (e.g., Feng et al., 2020; Wang & Tape, 2014), body wave tomography (e.g., Gou et al., 2019), Pn tomography (e.g., He & Lü, 2021), and receiver functions (Schulte-Pelkum et al., 2020).

A complete surface wave dispersion database across Alaska and the Alaska-Aleutian subduction zone, including Rayleigh and Love wave isotropic phase speed and azimuthal anisotropy, however, has not yet been produced.

The purpose of this study is to produce this database. This database is designed to be a basis for a 3-D seismic shear wave velocity model, which will also resolve detailed anisotropic properties of the crust and uppermost mantle. This database may be used alone or in concert with other types of data (e.g., receiver functions, body wave travel time measurements, shear wave splitting, gravity).

The asynchronous deployment of various seismic networks, as well as the noisy ocean bottom environment, provide challenges to the production of the surface wave database. These challenges have motivated the development of a new method of ambient noise interferometry based on observations at three stations at a time, called *three-station interferometry* (Zhang et al., 2020). Traditional two-station interferometry (Shapiro & Campillo, 2004) extracts information between two synchronously deployed stations, which leads to ambient noise tomography (e.g., Sabra et al., 2005; Shapiro et al., 2005). Three-station interferometry (e.g., Curtis & Halliday, 2010; Stehly et al., 2008) can bridge asynchronous seismic stations (e.g., Curtis et al., 2012; Ma & Beroza, 2012) by using the correlation of coda or correlation/convolution of direct waves observed on two-station interferograms. Compared with two-station interferometry and three-station coda interferometry, three-station direct-wave interferometry has been shown to improve the signal-to-noise ratio (SNR) of surface wave dispersion measurements significantly, by accentuating the coherent waves propagating between stations with interferometry and then stacking (Zhang et al., 2020, 2021). The resulting three-station measurements exist for both synchronously and asynchronously deployed stations. Thus, many more measurements are made using three-station interferometry, which improves the resolution of the dispersion maps (e.g., Chen & Saygin, 2020; Spica et al., 2016; Zhang et al., 2020, 2021).

Here, we present a comprehensive surface wave dispersion database across Alaska and the Alaska-Aleutian subduction zone, applying the new three-station direct-wave interferometry (Zhang et al., 2020, 2021) as well as two-station interferometry and earthquake tomography (e.g., Lin & Ritzwoller, 2011b). The final product merges measurements of all methods into a composite data set that contains Rayleigh wave isotropic phase speed and phase speed azimuthal anisotropy at periods ranging from 8 to 85 s, as well as Love wave isotropic phase speed at periods from 8 to 80 s. We do not measure Love wave phase speed azimuthal anisotropy (with mainly 4ψ anisotropy and 90° periodicity) in this study. This is because it is harder to estimate reliably due to the need to add more azimuthal bins, which would increase the size of the uncertainty in each bin. Our data set is developed as a basis for inferring the depth-dependent 3-D isotropic and anisotropic crustal and mantle structure in Alaska onshore and offshore, as the basis for future work.

The paper is structured as follows. In Section 2, we describe the data processing and measurement procedures and characteristics for both ambient noise (two- and three-station interferometry) and earthquakes. We discuss the tomographic methods and uncertainty estimation in Section 3. Section 4 presents the composite tomographic maps of Rayleigh and Love wave isotropic phase speed and Rayleigh wave azimuthal anisotropy. Finally, we discuss the difference in results determined from different methods, compare our composite results with previous studies, and highlight the azimuthal anisotropy pattern observed for the Alaska-Aleutian subduction zone (Section 5).

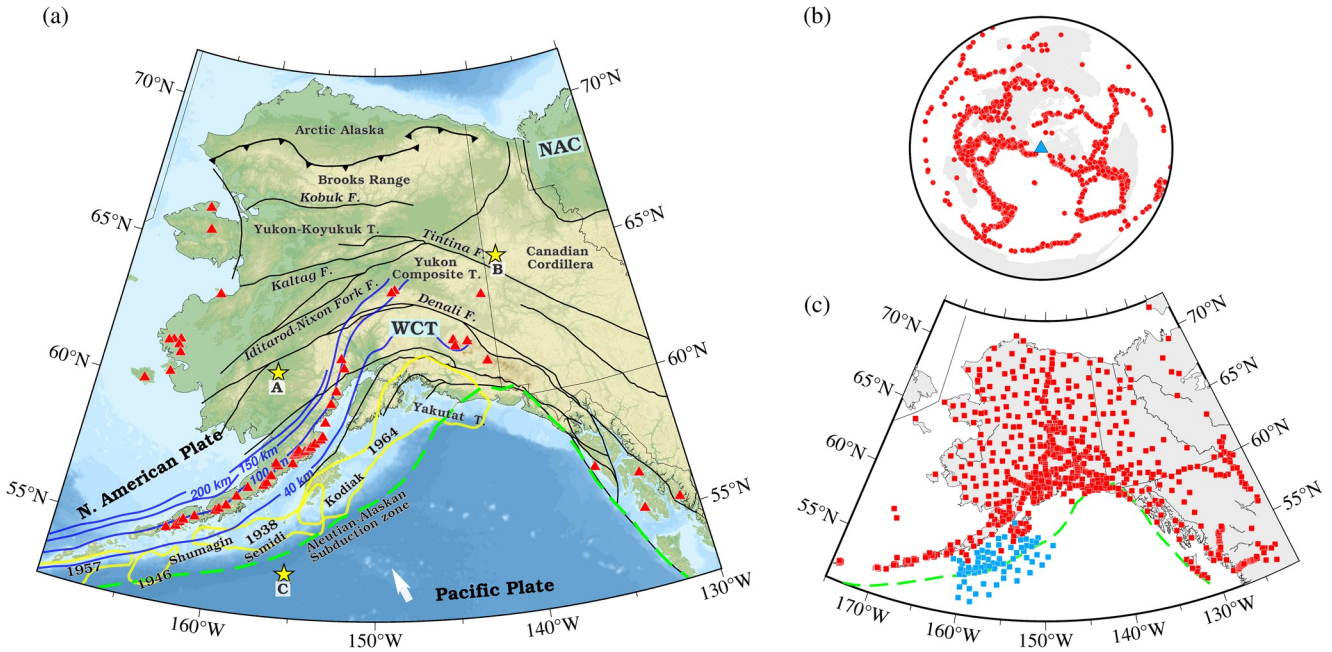

Figure 1. Alaska tectonics, earthquakes used, and seismic stations. (a) Tectonic map of Alaska. The black curves are major faults (ending with "F."). The four blue contours show the surface of the Aleutian-Alaskan slab at different depths (40, 100, 150, and 200 km), based on the Slab2.0 model (Hayes et al., 2018). The red triangles denote volcanoes. Major tectonic terranes, mountain ranges, and faults (Colpron et al., 2007) are labeled. NAC = North American Craton and WCT = Wrangellia composite terrane. Yellow stars represent the example points used in Figures 4 and 8. The white arrow indicates the direction of motion of the Pacific Plate. The yellow polygons show the rupture zones of previous megathrust earthquakes (Tape & Lomax, 2022). The green dashed line shows the plate boundary between the Pacific and North American Plates. (b) Locations of earthquakes used. Red dots show the earthquakes (date range: January 2000–October 2020; $M_s > 5.5$, signal-to-noise ratio > 10; 3,395 events shown here) used in this study (see Section 2.2 for details). (c) Station distribution: red squares for onshore stations and blue squares for ocean bottom seismometers from the Alaska Amphibious Community Seismic Experiment.

2. Constructing Interferograms and Making Dispersion Measurements

The seismic stations used in this study extend from northwest Canada, across Alaska, and offshore of the Alaska Peninsula, deployed from January 2000 to October 2020. There are 979 seismic stations used in total (Figure 1b), including 75 ocean bottom seismometers (OBS) from the AACSE. The AACSE OBS stations were deployed from May 2018 through August 2019 and were synchronous with most of the land stations. The average station spacing is ~80 km (Figure S1 in Supporting Information S1).

2.1. Ambient Noise Data

We use ambient noise data both in traditional two-station ambient noise interferometry as well as the new three-station interferometry. We follow the notation of Zhang et al. (2020) to describe the three interferometric methods used in this study:

1. I_2: Traditional two-station interferometry,
2. I_3^{ell}: Three-station interferometry with source-stations in an elliptical stationary phase zone between the two receiver stations, and
3. I_3^{hyp}: Three-station interferometry with source-stations in a hyperbolic stationary phase zone radially outside the two receiver stations.

2.1.1. Two-Station Interferometry

In two-station interferometry, ambient noise data are processed differently for land and OBS stations. For land stations, we follow a traditional procedure (e.g., Bensen et al., 2007; Feng & Ritzwoller, 2019) for both vertical-vertical (ZZ) and transverse-transverse (TT) components. This includes (a) applying temporal and spectral normalizations to broaden the usable bandwidth and diminish the effect of spatially localized sources (such as earthquakes) and (b) computing daily cross-correlations and stacking over days for all

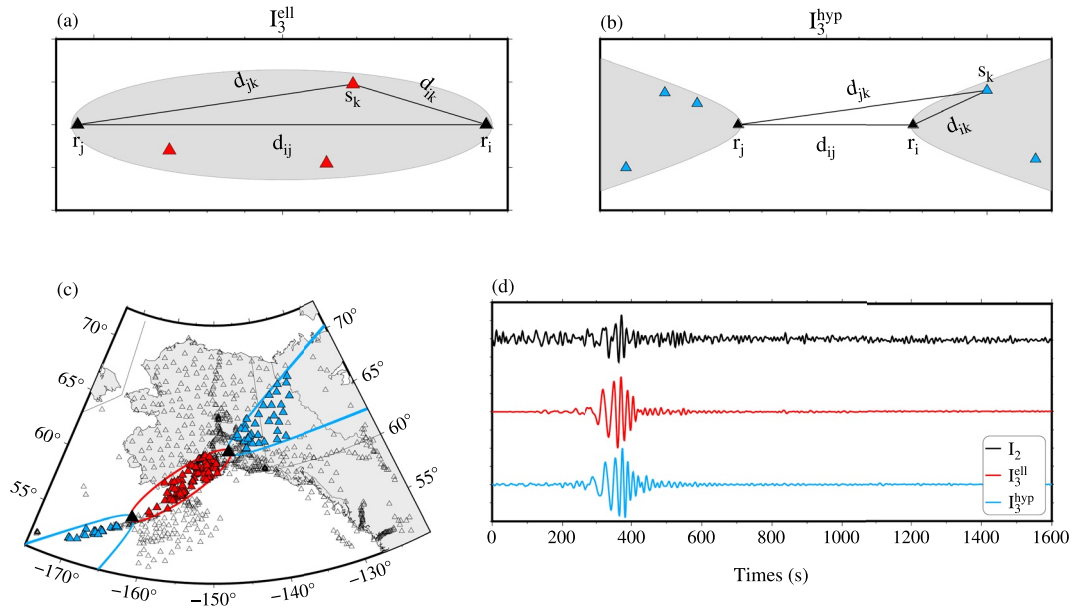

Figure 2. Schematic illustration and example application of three-station interferometry. (a) For the three-station method, I_3^{ell}, all source-stations must lie within an elliptical stationary phase zone (gray shading) with two receiver-stations (r_i and r_j) as foci. (b) Similar to (a), but for the three-station method, I_3^{hyp}, in which all source-stations must lie within a hyperbolic stationary phase zone (gray shading). (c) Example of stationary phase zone constraints on source-stations (blue and red triangles) for the receiver-station pair, TA.S12K-AK.SCM (black triangles). The red ellipse indicates the stationary phase zone of I_3^{ell} with the corresponding source-stations marked in red. The blue hyperbola outlines the stationary phase zone of I_3^{hyp} with corresponding source-stations marked in blue. This example includes 109 and 82 source-stations for the I_3^{ell} and I_3^{hyp}, respectively. (d) Comparison of Z-Z component waveforms for I_2, I_3^{ell}, and I_3^{hyp} for the receiver-station pair TA.S12K-AK.SCM. Corresponding source-stations for I_3^{ell} and I_3^{hyp} are color-coded and shown in panel (c).

synchronously deployed station-pairs. For OBS stations, before applying the same preprocessing to continuous vertical component records, we reduce the tilt and compliance noise from vertical components using transfer functions from the horizontal components and the differential pressure gauge, respectively (e.g., Bell et al., 2015; Crawford & Webb, 2000; Janiszewski et al., 2019; Tian & Ritzwoller, 2017). Finally, we average the causal and acausal lags of the stacked correlations to obtain the symmetric components for both ZZ and TT components of land station pairs and the ZZ component for OBS-OBS or OBS-land station pairs. These symmetrized two-station interferograms also form the basis for three-station interferometry (Section 2.1.2).

2.1.2. Three-Station Interferometry

We follow Zhang et al. (2020, 2021) in performing three-station direct-wave interferometry. Three-station interferometry has two flavors based on source station locations: I_3^{ell} and I_3^{hyp} (Figures 2a and 2b).

First, we define a stationary phase zone (Snieder, 2004), which imposes a geometrical constraint on the relationship between the stations used. Consider two receiver-stations, r_i and r_j, which are separated by a distance d_{ij}, and a source-station s_k which lies a distance d_{ik} from r_i, and d_{jk} from r_j (Figures 2a and 2b). For the method I_3^{ell}, let δd^{ell} represent the distance difference between the sum of source-receiver distances and the inter-receiver distance (Figure 2a),

$$\delta d^{ell} = |d_{ik} + d_{jk}| - d_{ij}. \quad (1)$$

For the method I_3^{hyp}, let δd^{hyp} represent the distance difference between the differential source-receiver distances and the inter-receiver distance (Figure 2a),

$$\delta d^{hyp} = |d_{ik} - d_{jk}| - d_{ij}. \quad (2)$$

The stationary phase zone for both flavors is defined as (Zhang et al., 2021):

$$|\delta d| < d_\alpha, \tag{3}$$

where d_α is an ad hoc distance factor. We choose $d_\alpha = 30$ km in this study. The stationary phase zone is an ellipse for I_3^{ell} (Figure 2a), and a hyperbola for I_3^{hyp} (Figure 2b). Because I_2 signals are unreliable for inter-station distances less than one wavelength (Zhang et al., 2021), λ, we follow Zhang et al. (2021) to apply a cut-off wavelength for the longest usable period:

$$\min(d_{ik}, d_{jk}) > \lambda_{\max}, \tag{4}$$

where $\lambda_{\max} = 200$km for the longest period at 50 s with an approximate phase speed of 4 km/s. Figure 2c shows an example of the stationary phase zones for both I_3^{ell} and I_3^{hyp}, and the corresponding source-stations within the stationary phase zones, for the receiver-station pair of TA.S12K-AK.SCM.

In addition to the geometrical constraint on the location of the source-stations, s_k, we only accept a source-station when the SNR of both $I_2(r_i, s_k)$ and $I_2(r_j, s_k)$ are greater than 10. SNR is defined as the ratio of peak amplitude divided by the RMS of trailing noise (Bensen et al., 2007). After applying the criteria mentioned above, the average number of source-stations of I_3^{ell} and I_3^{hyp} are 21 and 40 for Rayleigh waves and 17 and 33 for Love waves, respectively.

Source-specific three-station interferograms, $C_3(r_i, r_j; s_k)$, are constructed either by correlation or convolution of the two-station interferograms $I_2(r_i, s_k)$ and $I_2(r_j, s_k)$. For I_3^{ell}, where the source-station s_k is in the elliptical stationary phase zone, $I_2(r_i, s_k)$ and $I_2(r_j, s_k)$ are convolved; but for I_3^{hyp}, when the source-station s_k is in the hyperbolic stationary phase zone, $I_2(r_i, s_k)$ and $I_2(r_j, s_k)$ are correlated. Composite estimated Green's functions between receiver stations r_i and r_j, $\widehat{G_3}(r_i, r_j)$, are constructed by a weighted stacking over phase-shifted source-specific interferograms, $\widetilde{C_3}(r_i, r_j; s_k)$, from N contributing source-stations:

$$\widehat{G_3}(r_i, r_j) \equiv \sum_{k=1}^{N} w_{i,j;k} \widetilde{C_3}(r_i, r_j; s_k), \tag{5}$$

where $w_{i,j;k}$ is the weight defined by the reciprocal of the RMS of the trailing noise in the interferogram $\widetilde{C_3}$, and $\widetilde{C_3}$ is the phase-shifted C_3 accounting for the geometrical debias in phase speed measurement (Zhang et al., 2021). In particular,

$$\widetilde{C_3} = \mathcal{F}^{-1}\left[\mathcal{F}[C_3] \cdot e^{\frac{i\omega\delta d}{c_{\text{ref}}}}\right], \tag{6}$$

where $\mathcal{F}$ and $\mathcal{F}^{-1}$ are the Fourier transform and its inverse, respectively, c_{ref} is a reference inter-receiver phase speed, and δd is defined by Equations 1 and 2, in which ${}^{ell}\delta d \geq 0$ for I_3^{ell}, ${}^{\text{hyp}}\delta d \leq 0$ for I_3^{hyp}, respectively. c_{ref} between receiver-stations r_i and r_j is estimated from the tomography results of I_2 at the corresponding periods.

Figure 2d compares the example composite estimated Green's functions for I_2, I_3^{ell}, and I_3^{hyp}, for the receiver-station pair TA.S12K-AK.SCM. The amplitudes of precursory noise and trailing noise for I_3^{ell} and I_3^{hyp} are typically lower than those of I_2.

2.2. Earthquake Data

Broadband waveforms from 3,395 teleseismic earthquakes recorded at 979 seismic stations with $M_s > 5.5$ that occurred between January 2000 and October 2020 are also used to produce Rayleigh and Love wave dispersion measurements (Figure 1b). The vertical components of earthquake waveforms recorded by the OBS are pre-processed similarly to OBS ambient noise data described in Section 2.1.1, including denoising of vertical components of compliance and tilt noise. For each earthquake record and period, we apply automatic frequency-time analysis (FTAN; e.g., Levshin & Ritzwoller, 2001), described in Section 2.3, to measure both the phase traveltime and amplitude of Rayleigh and Love waves. We discard the measurements if the corresponding SNR is less than 10. In Section 5.1, earthquake data are compared with ambient noise data at intermediate periods

for validation. Moreover, earthquakes observations complement ambient noise-based observations at long periods and a wide spatial-distribution of earthquakes provides complementary azimuthal coverage to ambient noise data where station spacing is sparse.

2.3. Dispersion Measurements

We obtain measurements of Rayleigh and Love wave phase speeds by FTAN (e.g., Bensen et al., 2007; Levshin & Ritzwoller, 2001). Theoretically, the phase of the estimated Green's function with instantaneous frequency ω observed at time t can be expressed as follows (e.g., Lin et al., 2008):

$$\phi(\omega, t) = \omega \frac{d}{c} - \omega t + \frac{\pi}{4} + n \cdot 2\pi + \phi_s, \tag{7}$$

where d is the interstation distance for ambient noise data and the epicentral distance for earthquake data, c is the phase speed at a given frequency ω, $\frac{\pi}{4}$ accounts for the phase shift between the displacement response and the applied force plus the phase shift due to the far-field approximation of Bessel functions, $n \cdot 2\pi$ is the intrinsic ambiguity in the phase measurement when n is an integer, and ϕ_s is an initial phase ambiguity term.

For earthquake data, the initial phase term ϕ_s is determined by the focal mechanism. For earthquake tomography, we measure differences in traveltime field, thus ϕ_s cancels approximately. For two-station ambient noise interferometry, ϕ_s is set to zero, consistent with observations of Lin et al. (2008).

For three-station interferometry, the initial phase term ϕ_s must include the effects of correlation/convolution (Zhang et al., 2020). Following Zhang et al. (2021), we summarize the choices of the initial phase term ϕ_s as followed:

$$\phi_s = \begin{cases} 0 & \text{for } I_2, \\ \frac{\pi}{4} & \text{for } I_3^{\text{ell}}, \\ -\frac{\pi}{4} & \text{for } I_3^{\text{hyp}}. \end{cases} \tag{8}$$

An example comparison of Rayleigh wave phase speed dispersion curves is shown in Figure S2 in Supporting Information S1.

SNR is an important indicator of the quality of the dispersion measurements, and we use it as a data selection criterion. Figures 3a and 3b compares the medians of the SNR of the measurements from ambient noise and earthquake data for both Rayleigh and Love waves. For the ambient noise methods, on average, I_3^{ell} and I_3^{hyp} improve SNR over traditional two-station interferometry by factors of ∼1.7 and ∼2.4, respectively, for both Rayleigh and Love waves. For the Rayleigh wave, SNR for I_2 shares similar trends with I_3^{ell} and I_3^{hyp}, peaking near or just above the secondary (∼8 s) and primary (∼16 s) microseisms, respectively, and dropping at longer periods. For the Love wave, the SNR curves for ambient noise data only exhibit a single peak and decrease quickly above 16 s period. For both Rayleigh and Love waves, I_3^{hyp} yields much higher SNR measurements than that of I_3^{ell}, because about double the number of source-stations are stacked for I_3^{hyp} than for I_3^{ell} for the seismic station configuration of this study. The SNR for earthquake measurements remains higher than for I_2 at long periods, whereas it drops relatively rapidly at shorter periods for both Rayleigh and Love waves.

Figures 3c and 3d compares the number of paths for the different methods after quality control, which requires the SNR of measurements to be larger than 10 for all methods and inter-station distances to be greater than one wavelength at each period for the ambient noise measurements. For the ambient noise measurements of both Rayleigh and Love waves, both three-station interferometry methods, I_3^{ell} and I_3^{hyp}, yield about twice the number of paths of I_2 on average, due to their ability to bridge asynchronous receiver-station pairs and to improve the SNR of the measurements rejected by I_2 due to low SNR. At short periods, the number of paths from earthquake measurements is smaller than that from ambient noise methods. However, at periods above 30 s, the number of paths from earthquakes is larger than from ambient noise methods. This results in good complementarity of earthquake measurements compared with the ambient noise data set, especially at long periods.

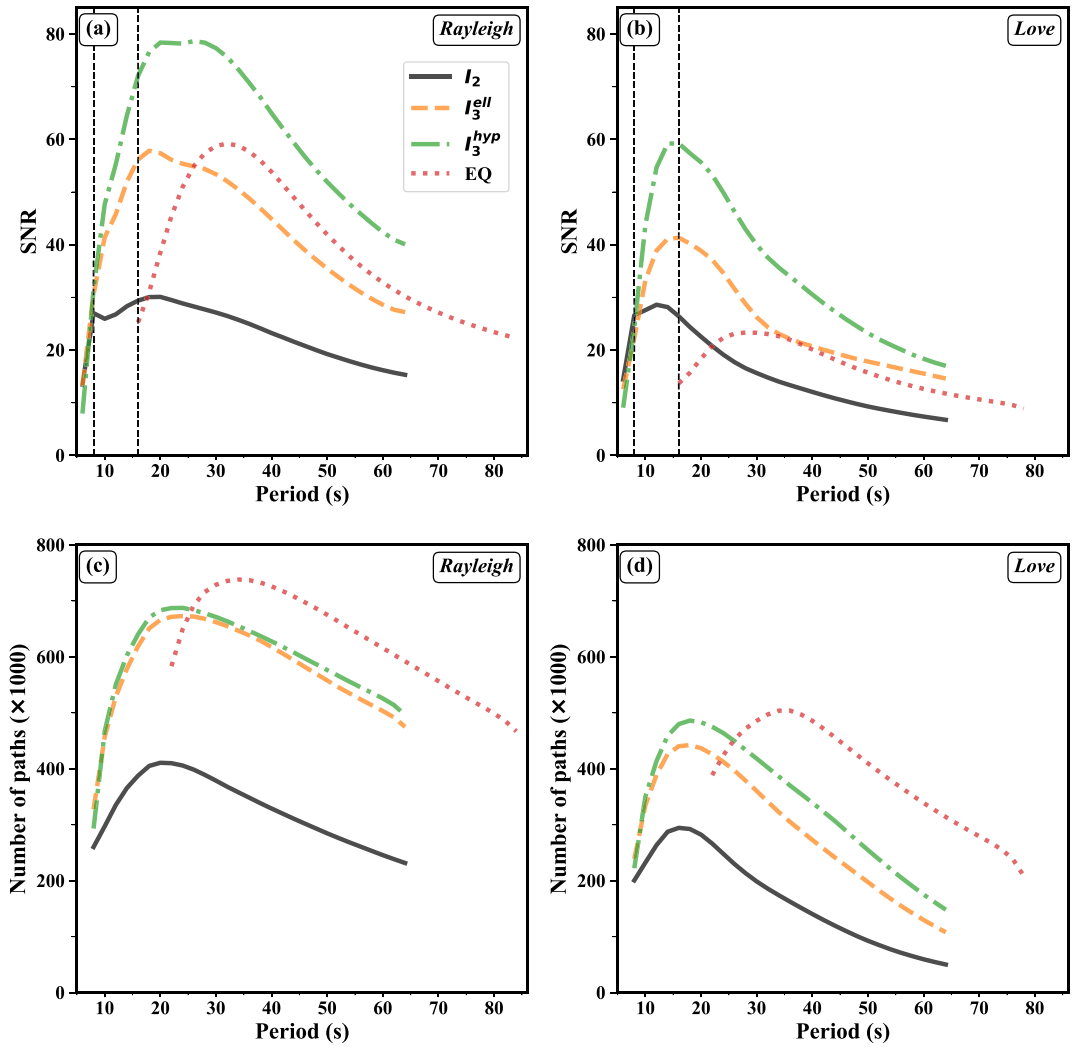

Figure 3. The signal-to-noise ratio (SNR) and number of paths for Rayleigh and Love waves. (a, b) SNR as a function of the period for I_2, I_3^{ell}, I_3^{hyp}, and earthquake (EQ) measurements for (a) Rayleigh waves and (b) Love waves. Vertical dashed lines indicate the globally dominant ocean microseisms at 8 and 16 s. (c, d) Similar to (a, b), except for the number of measurements. For earthquake and ambient noise recorded in Alaska, we use ambient noise measurements only at 50 s period and below, but show information about them here to 65 s period, and we use earthquake measurements only at 28 s period and above.

3. Surface Wave Maps

3.1. Eikonal and Helmholtz Tomography

With densely deployed seismic stations arrayed both onshore and offshore in Alaska, we estimate the local phase speed and the related azimuthal anisotropy directly from the spatial derivatives of the wavefield traveltime measurements, rather than via traditional path-based tomography that requires ad hoc smoothing constraints to regularize the linear inverse problem (e.g., Barmin et al., 2001). In this way, we apply eikonal tomography for ambient noise data (Lin et al., 2009) and Helmholtz tomography for earthquake data (Lin & Ritzwoller, 2011b).

For Helmholtz tomography with earthquake data, the 2D phase traveltime and amplitude fields for the *i*th actual source can be interpreted as follows:

$$\frac{1}{c_i(\boldsymbol{r})^2} = |\nabla \tau_i(\boldsymbol{r})|^2 - \frac{\nabla^2 A_i(\boldsymbol{r})}{A_i(\boldsymbol{r})\omega^2}, \tag{9}$$

where ω is frequency, $\tau_i(\boldsymbol{r})$, $c_i(\boldsymbol{r})$, and $A_i(\boldsymbol{r})$ are the local traveltime, phase speed, and amplitude at position $\boldsymbol{r}$. For eikonal tomography with ambient noise data, we drop the right-hand side amplitude term, which is appropriate when the spatial variation of the amplitude is smooth, or the frequency is high. Then, for the ith virtual source we have

$$\frac{\hat{k}_i}{c_i(\boldsymbol{r})} \cong \nabla \tau_i(\boldsymbol{r}), \tag{10}$$

where $\hat{k}_i$ is the unit wave number vector describing the direction of propagation of the wave (azimuth, ψ). Helmholtz tomography requires amplitude information, which is preserved in the processing of earthquake data but is lost in ambient noise data processing and can provide a more accurate estimate of phase speed, partially accounting for finite frequency effects. In total, ~3,000 earthquakes are used in Helmholtz tomography across the 979 stations. Both Helmholtz and eikonal tomography are performed on a 0.2°(longitude) by 0.1° (latitude) grid (~11 km). Because amplitude information is lost in the ambient noise data processing, we perform eikonal tomography for ambient noise data.

Eikonal and Helmholtz tomography each provide measurements of local phase speed $c_i(\boldsymbol{r})$ at location $\boldsymbol{r}$ from source i (either an earthquake or virtual source station for ambient noise) propagating in direction $\hat{k}_i$. These measurements at each location are then used to estimate isotropic and azimuthally anisotropic phase speed.

For both Rayleigh and Love waves, we measure isotropic phase speed on a spatial grid with a spacing of about 11 km. At periods from 8 to 50 s, measurements are derived from eikonal tomography for the ambient noise methods, I_2, I_3^{ell}, and I_3^{hyp}. In addition, at periods from 28 to 85 s, the phase speed measurements are derived from Helmholtz tomography applied to earthquake data. For Love waves, the measurements are averaged at each grid point and period to provide an estimate of isotropic phase speed. The measurement procedure for Rayleigh waves is described in Section 3.2.

For different input data (I_2, I_3^{ell}, I_3^{hyp}, and earthquake data) and for eikonal and Helmholtz tomography, phase speed estimates, $c_i(\boldsymbol{r})$, at each location (and azimuthal direction) are combined. The raypath density maps for Rayleigh and Love wave composite results are shown in Figure S3 and S4 in Supporting Information S1, respectively.

3.2. Rayleigh Wave Phase Speed Azimuthal Anisotropy

For the Rayleigh wave, we also consider the directional (azimuthal) dependence of phase velocity directly from measurements of local phase speed $c(\boldsymbol{r}, \psi)$ propagating in different directions. In weakly anisotropic media, we parametrize Rayleigh wave phase speed for azimuth ψ (Smith & Dahlen, 1973),

$$c(\psi) = c_{\text{iso}}\left(1 + \frac{A_1}{2}\cos(\psi - \psi_1) + \frac{A_2}{2}\cos 2(\psi - \psi_2)\right), \tag{11}$$

where, c_{iso} is the isotropic phase speed, ψ_1 and ψ_2 are the fast axes for the 1ψ and 2ψ components of anisotropy, A_1 and A_2 are the peak-to-peak relative amplitudes for the 1ψ and 2ψ anisotropy, respectively.

The 1ψ anisotropy, with 360° periodicity, is not caused by intrinsic anisotropy (Lin & Ritzwoller, 2011a; Smith & Dahlen, 1973), and was not included in the equation of Smith and Dahlen (1973). We estimate both 1ψ and 2ψ anisotropy simultaneously in this study at periods above 50 s to remove the non-anisotropic 1ψ bias. This is discussed further in Section 4.3.

To improve estimates of the azimuthal anisotropy of Rayleigh wave phase speed, we perform azimuthal stacking and binning (Lin et al., 2009). For stacking, we apply a spatial averaging based on a coarse spatial grid with a spacing of about 130 km to bring in more measurements and improve azimuthal coverage compared with the original fine grid, as illustrated in Figure S5 in Supporting Information S1. We treat every point on the fine grid as a central point, and measurements are accumulated on that grid from the nearest eight surrounding points on the coarse spatial grid. To reduce the impact of small-scale, sub-grid spacing isotropic phase speed heterogeneity, we employ phase speed perturbations, defined as follows. The ith azimuthally dependent phase speed perturbation from surrounding or central point j on the coarse grid for a given central point is written as:

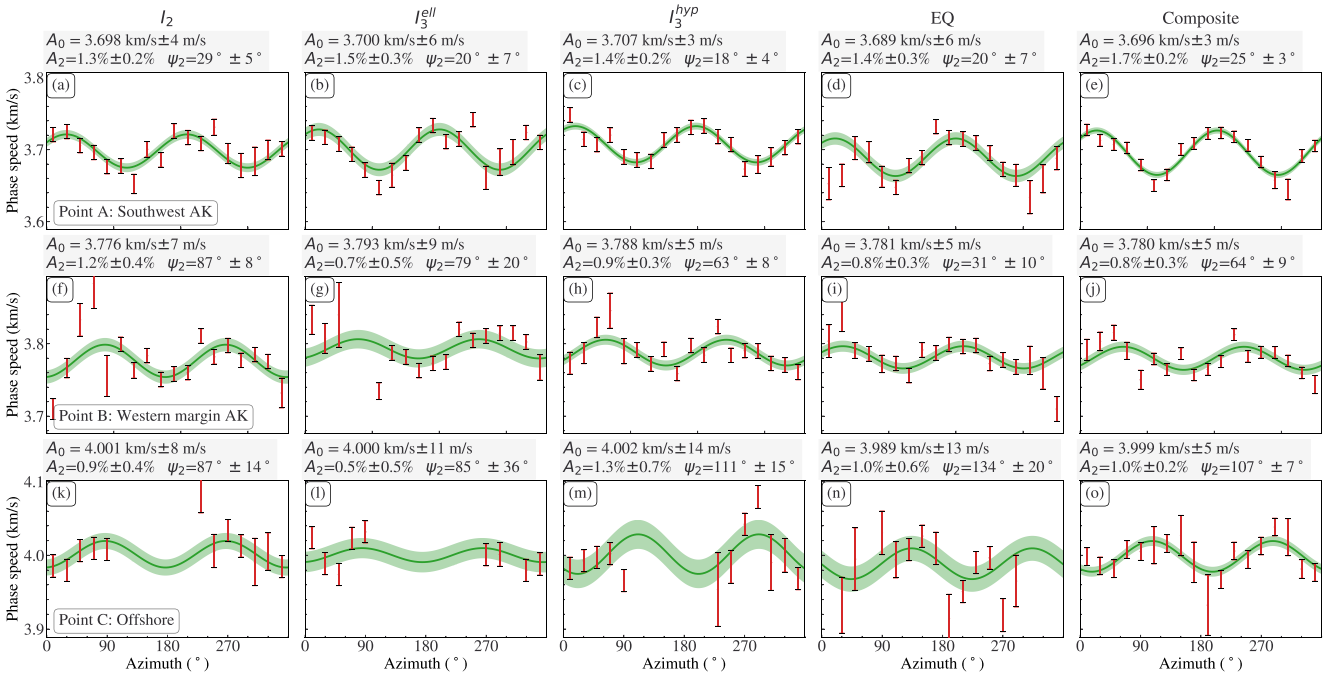

Figure 4. Examples of Rayleigh wave phase speed measurements binned over azimuth (red bar) at 30 s period and their 2ψ least squares fit (green lines). Three different locations are shown (rows) using different methods (columns). Points A, B, and C are identified in Figure 1a. Error bars are mean ± one standard deviation of the mean. The green shadow indicates the uncertainty of the best-fit line, which is estimated by the linear propagation of uncertainty. Azimuth is defined as degrees clockwise from north.

$$\Delta c_{ij}(\psi) = c_{ij}(\psi) - \overline{c}_j, \tag{12}$$

where $\overline{c}_j$ is the mean phase speed at point j. Then, for binning, we compute the mean and standard deviation of the mean in each 20° azimuthal bin (18 bins in total) using all of the measurements of perturbations (Equation 12) plus the mean of the phase speed at a central point in each bin. This process increases the number of measurements for each azimuthal bin at the expense of decreasing the spatial resolution of azimuthal anisotropy (Lin et al., 2009), which results in a lower resolution of the coarse grid (~130 km) for azimuthal anisotropy in comparison with the resolution for isotropic structure on the fine grid (~80 km).

At each grid and each period, using the observations of phase speed and corresponding uncertainties at each azimuthal bin acquired from stacking and binning, we apply a least squares linear fit based on Equation 11 to estimate the isotropic Rayleigh wave phase speed and azimuthal anisotropy (c_{iso}, A_1, A_2, ψ_1, and ψ_2) with corresponding uncertainties at each fine grid location. The uncertainty estimates for the unknowns are derived from the corresponding covariance matrix based on linear error propagation (Lebigot, 2022). We show examples of the predicted curve, $c(\psi)$, based on Equation 11 in Figure 4, which we discuss further in Section 5.1.1. The corresponding corridor of the uncertainty of $c(\psi)$ is also estimated by using linear error propagation.

3.3. Quantification of the Uncertainty of Phase Speed Measurements

Accurate uncertainty estimates of phase speed measurements are important in the inversion for a 3-D model of isotropic and anisotropic structures. To determine if our uncertainty estimates for c_{iso}, A_1, A_2, ψ_1, and ψ_2 are accurate, we investigate two metrics of accuracy: (a) if the fit curve, $c(\psi)$, agrees with the binned measurements within the uncertainties and (b) if results from the different methods agree within the uncertainties. Both metrics are applied to Rayleigh waves and only the second to Love waves. Also, initially, for Rayleigh waves we apply a lower threshold or floor to all uncertainty measurements, so that for each of the 18 azimuthal bins at each grid point uncertainties are not smaller than 15 m/s for the offshore region (south of 60°N and west of 145°W) and 10 m/s onshore.

First, as for the first metric, we consider the misfit of the fit curve, $c(\psi)$, to the binned phase speed measurements. Misfit is defined here as the square root of reduced chi-squared between the estimated and observed phase speed at location $\boldsymbol{r}$, that is holding period constant:

$$S(\boldsymbol{r}) = \left[\frac{1}{N}\sum_{i=1}^{N}\left(\frac{c(\psi_i)^{\text{obs}} - c(\psi_i)^{\text{pred}}}{\sigma_i}\right)^2\right]^{1/2}, \tag{13}$$

where $c(\psi_i)^{\text{obs}}$ is the observed phase speed at azimuth ψ_i, $c(\psi_i)^{\text{pred}}$ is the predicated phase speed based on Equation 11, σ_i is the uncertainty estimate for $c(\psi_i)^{\text{obs}}$, i is the azimuthal bin index, and N is the number of azimuthal bins, 18. On average, we find the misfit, $S(\boldsymbol{r})$, is larger than 1, but varies with both period and geographical location. The average value of misfit varies from 1.1 to 1.9, as a function of period. For instance, the spatially averaged misfit is about 1.6 for 30 s period Rayleigh wave.

We believe a misfit value larger than unity probably reflects the underestimation of the uncertainty of the binned phase speed measurements. Increasing these uncertainties will proportionately increase uncertainties in the fit variables for c_{iso}, A_1, A_2, ψ_1, and ψ_2. Therefore, we multiply the initial uncertainty estimates for these variables by the misfit, $S(\boldsymbol{r})$, at each location and period if it is larger than 1.

Second, we account for disagreement between the different methods by introducing an additional increase to the uncertainty estimates. By the analysis of the spatial standard deviation of the normalized difference between each pair of maps using different methods, we find the uncertainty estimates for Rayleigh and Love wave isotropic phase speed are underestimated by factors of 1.4 and 3.0, respectively (Appendix A). We believe the differences in phase speeds produced by different methods are due to the systematic errors caused by different sensitivity kernels for the different methods. Therefore, we further upscale the Rayleigh and Love wave isotropic phase speeds by factors of 1.4 and 3.0, respectively. This process of upscaling brings the methods into an agreement within the upscaled uncertainties.

In summary, let $\sigma_{\text{init}}(\boldsymbol{r})$ be an initial uncertainty estimate for a given period at position $\boldsymbol{r}$ for any of the variables, c_{iso}, A_1, A_2, ψ_1, or ψ_2. The final upscaled uncertainty estimate for that period, location, and variable is:

$$\sigma_{\text{final}}(\boldsymbol{r}) = \begin{cases} 1.4S(r)\sigma_{\text{init}}(r) & \text{for } c_{\text{iso}}^{\text{Rayleigh}}, \\ S(r)\sigma_{\text{init}}(r) & \text{for } A_1, A_2, \psi_1, \textit{and } \psi_2, \\ 3\sigma_{\text{init}}(r) & \text{for } c_{\text{iso}}^{\text{Love}}. \end{cases} \tag{14}$$

Examples of final upscaled uncertainties are shown in Figure 4, Figures S7, S9, and S12 in Supporting Information S1.

4. Composite Result

In the end, we obtain the final composite phase speed maps by stacking individual source-specific tomographic maps for both Rayleigh and Love waves, and for the Rayleigh wave, azimuthal anisotropy is resolved as well after the stacking.

4.1. Rayleigh Wave Isotropic Phase Speed Maps

At 10 s period (Figure 5a), only ambient noise data (I_2, I_3^{ell}, and I_3^{hyp}) are used in the tomography. At this period, Rayleigh wave phase speeds are primarily sensitive to the upper crustal structure, including sedimentary basins onshore and the accretionary wedge offshore. For onshore Alaska, the Colville Basin, the Yakutat Basin, and the Cook Inlet Basin are delineated as slow phase speed anomalies. In the offshore region, the accretionary wedge near the trench is marked by slow phase speed anomalies.

At 30 s period (Figure 5b), we use both ambient noise and earthquake data. The Rayleigh wave phase speeds at this period are mainly related to shear wave velocities in the middle and lower crust and crustal thickness. The

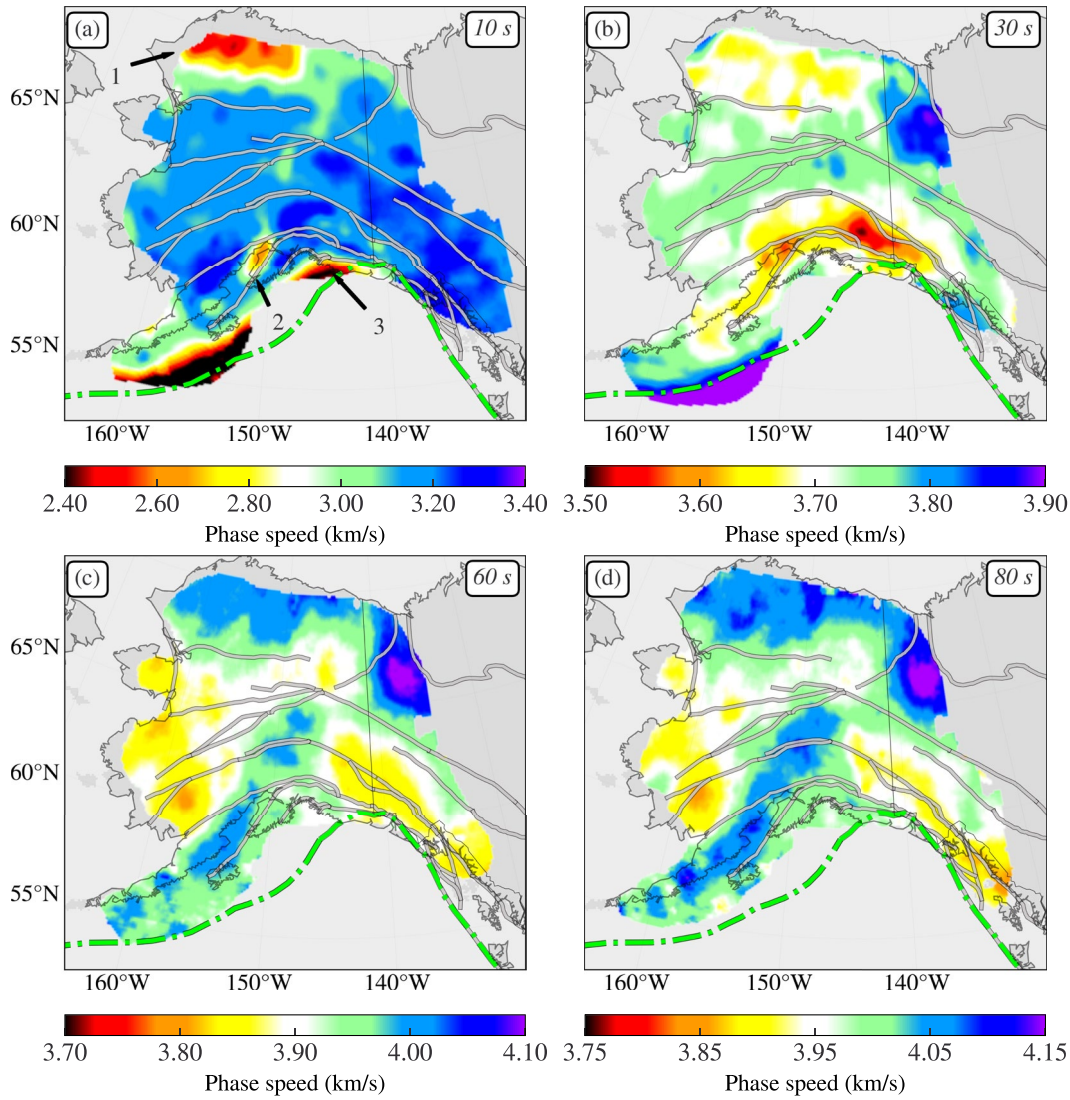

Figure 5. Rayleigh wave isotropic composite phase speed maps at periods of (a) 10, (b) 30, (c) 60, and (d) 80 s. Local faults are marked by gray lines. At 10 s period, arrows indicate sedimentary basins characterized by low-speed anomalies for 1: the Colville Basin; 2: the Cook Inlet Basin; and 3: the sedimentary strata overlying the Yakutat microplate. (a). The north American-Pacific Plate boundary is marked by the green dashed line.

slow anomalies in the Colville Basin and south Alaska reflect thicker crust in these regions in contrast with central Alaska, which has a shallower crust. The high phase speed anomalies in the northeast corner reflect the North American craton. For the offshore region, the outer-rise region stands out as a high phase speed anomaly along the trench due to the thinner crust.

At 60 and 80 s periods (Figures 5c and 5d), we use only earthquake data. Rayleigh wave phase speed is primarily sensitive to the uppermost mantle. The most striking feature at these periods is the subducted slab, which is delineated as a curved high-phase-speed anomaly, extending from the Aleutian peninsula to the south, along the volcanic arc, and ending northward of the Tintina fault. Another prominent feature is high-phase-speed anomalies in the north and northeast, which indicate the cratonic mantle roots beneath Arctic-Alaska and the North American craton. Rayleigh wave composite phase speed maps at more periods are shown in Figure S6 in Supporting Information S1.

The uncertainty analysis at the corresponding periods is shown in Figure S7 in Supporting Information S1. In general, uncertainties of the Rayleigh wave phase speed are less than 15 m/s for onshore Alaska, in contrast

with relatively larger uncertainties offshore. Uncertainties minimize near 30 s period both onshore and offshore, because both ambient noise and earthquake measurements exist at this period to yield a larger number of measurements. Above 30 s period, the average uncertainty increases because the number of measurements decreases.

4.2. Rayleigh Wave Azimuthally Anisotropic Maps

Rayleigh wave azimuthal anisotropy for phase speed at different periods reflects the shear wave velocity azimuthal anisotropy at different depths. When we refer to azimuthal anisotropy here, including the fast axes and amplitudes, we mean 2ψ anisotropy, because the 1ψ component is not caused by intrinsic anisotropy. We focus on the anisotropic pattern across Alaska in this section and leave the discussion of azimuthal anisotropy in the offshore region to Section 5.2, where we present zoomed-in maps. We compare our results to those of Feng et al. (2020) in Section 5.3.

At 18 s period (Figure 6a), we use only ambient noise data (I_2, I_3^{ell}, and I_3^{hyp}) to estimate anisotropy. The amplitude of azimuthal anisotropy is relatively strong both onshore and offshore. Fast axes at this period are roughly parallel to the strike directions of the local faults on the continent. The consistency of fast axes with the strike of nearby faults is also found in the world, such as in Yunnan, China (e.g., Liu et al., 2019) and the Alps (e.g., Kästle, et al., 2021). Offshore, in the accretionary wedge region, fast axes show trench-parallel directions. We believe that the azimuthally anisotropic patterns at this period likely reflect the impact of brittle deformation in the upper crust (e.g., Crampin, 1984).

At 36 s period (Figure 6b), we use both ambient noise and earthquake data. The azimuthal fast direction pattern is similar to that at 18 s in general but with relatively weaker amplitudes. South of the Denali fault, the anisotropic amplitude decreases, and there is a slight counterclockwise rotation of fast axis directions compared to the 18 s period.

At 50 and 80 s periods (Figures 6c and 6d), only earthquake data are used. The azimuthal anisotropy at these periods largely reflects the properties of the uppermost mantle and subducted slab. At 50 s period, high amplitude anisotropy appears in central Alaska, with fast directions consistent with those at short periods. In regions near the subducted slab, we observe trench-perpendicular fast axis directions, which form a horizontally circular pattern when combined with the sub-parallel fast direction in the back-arc region. At 80 s period, the amplitude of azimuthal anisotropy is weaker (<2%) compared with shorter periods. Anisotropic fast directions within the subducting slab are approximately parallel to the curved slab. The horizontally circular fast axes pattern diminishes in the slab region. The results at more periods are shown in Figure S8 in Supporting Information S1.

The uncertainties of the fast azimuth direction and the amplitude for corresponding periods are shown in Figure S9 in Supporting Information S1.

4.3. Influence of Apparent 1ψ Anisotropy and Helmholtz Tomography

Strong 1ψ anisotropy (360° periodicity) has previously been observed in the Rayleigh wave earthquake tomographic studies in the western United States (Lin & Ritzwoller, 2011b) and Cascadia (Zhang et al., 2021). The existence of 1ψ anisotropy is thought to be caused by the unmodelled finite frequency effect of backward scattering (Lin & Ritzwoller, 2011a). We resolve both 1ψ and 2ψ anisotropy simultaneously in this study at periods above 50 s (only earthquake measurements) to remove this non-intrinsic 1ψ bias.

To suppress the effect of backward scattering, we perform Helmholtz tomography for earthquakes rather than eikonal tomography. The 1ψ anisotropy patterns resolved by using eikonal tomography and Helmholtz tomography for earthquakes are shown in Figures S10a–S10h in Supporting Information S1. We find that 1ψ anisotropy is prominent at long periods (above 50 s) near the boundaries of the strong isotropic phase speed contrasts, such as regions near the cratonic roots beneath Artic-Alaska and the North American craton, and near the subducted slab (Figures S10a–S10d in Supporting Information S1). The fast directions of 1ψ anisotropy point toward the high-speed anomalies. Compared with eikonal tomography, the application of Helmholtz tomography reduces the influence of 1ψ anisotropy (Figures S10e–S10h in Supporting Information S1) and the phase speed anomalies become more pronounced (Figures S10i–S10l in Supporting Information S1), such as the high-speed anomalies in the North American craton and the subducted slab. On average, the absolute deviation of isotropic speed

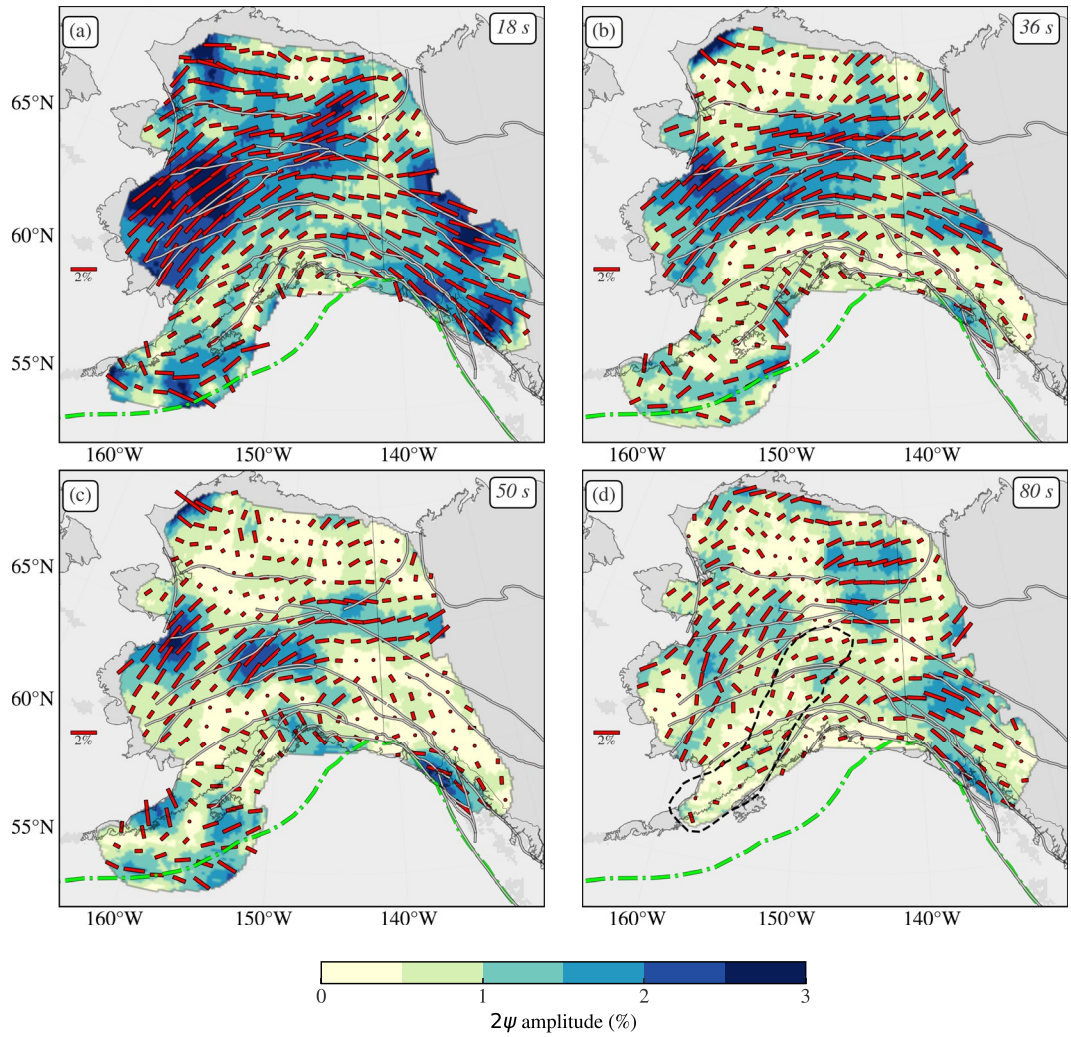

Figure 6. The amplitude and fast-axis directions for Rayleigh wave phase speed azimuthal anisotropy at periods of (a) 18, (b) 36, (c) 50, and (d) 80 s for the composite data set. The red bars indicate the fast directions of 2ψ anisotropy and the lengths are proportional to the amplitude A_2. The background map shows the value of A_2. The dashed line in panel (d) indicates the position of the subducted slab identified by the high-speed anomaly in Figure 5d.

between the results from Helmholtz tomography and eikonal tomography is around 10 m/s. We further reduce the effect of 1ψ anisotropy by fitting for it along with 2ψ anisotropy using Equation 11.

4.4. Love Wave Isotropic Phase Speed Maps

Compared with the Rayleigh wave phase speed at a given period, the Love wave phase speed at that period is more sensitive to shallower depths. Due to greater local noise and lower SNR on horizontal components, we only process the vertical seismic records for the OBS stations, resulting in no Love wave phase speed measurements from AACSE. Thus, the tomographic result of the Love wave phase speed is confined to onshore Alaska.

As with Rayleigh waves, at 10 and 20 s periods (Figures 7a and 7b), we only use ambient noise data (I_2, I_3^{ell}, and I_3^{hyp}). The Love wave phase speeds are primarily sensitive to the upper and middle crustal structures in the continental regions at these periods. The phase speed map at 10 s period resembles the high and low-speed anomalies at 20 s. Similar to the Rayleigh wave phase speed map at 10 s, the Colville Basin in Arctic Alaska, the sedimentary strata overlying the Yakutat microplate, and the Cook Inlet Basin are delineated as slow phase speed anomalies.

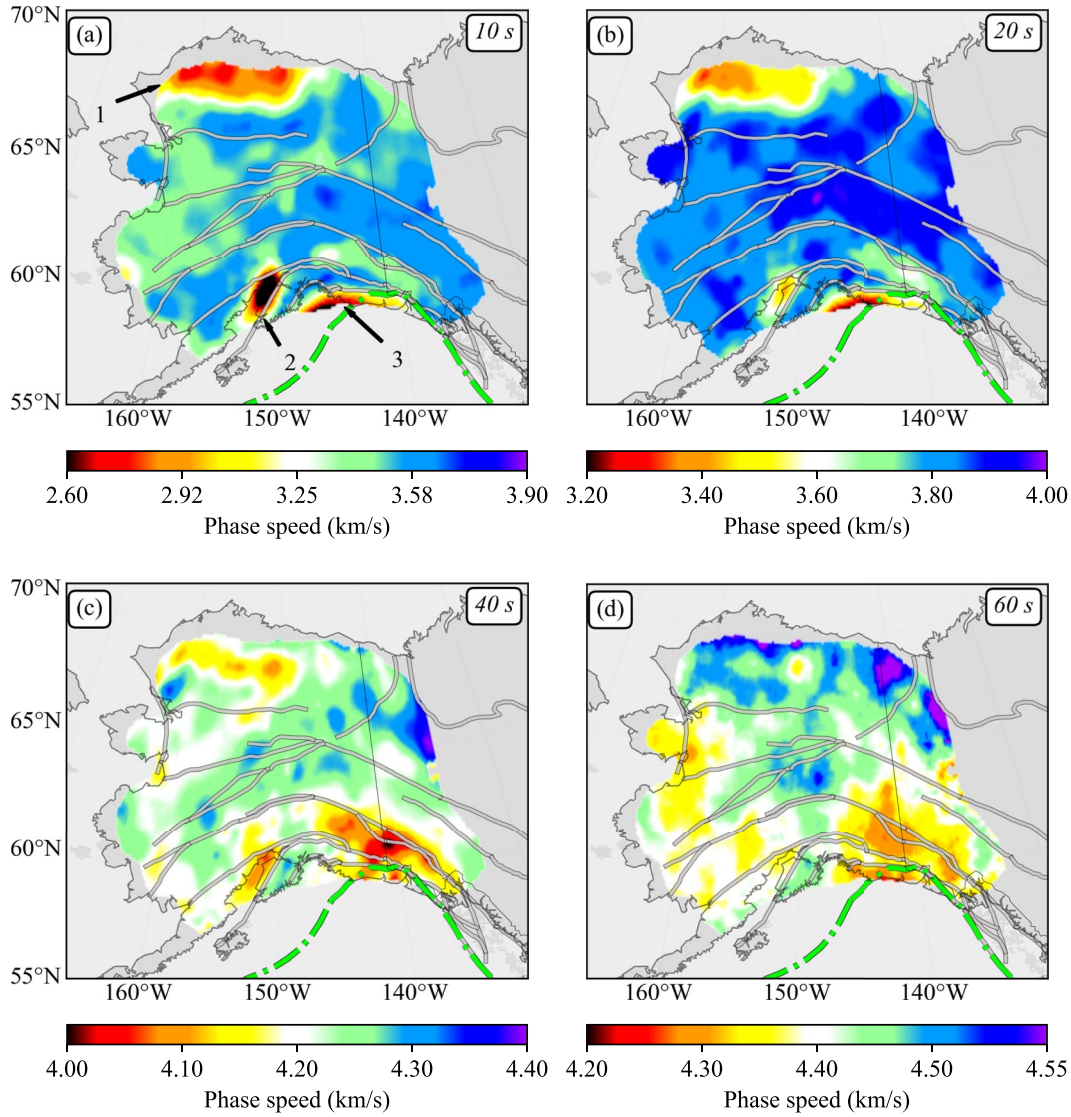

Figure 7. Love wave isotropic phase speed maps at periods of (a)10, (b) 20, (c) 40, and (d) 60 s for the composite data set. The gray and green lines are the same as in Figure 6.

At 40 s period (Figure 7c), the result is based on both ambient noise and earthquake data. The Love wave phase speeds largely reflect the shear wave speeds in the middle and lower crust and the influence of Moho depth (e.g., Christeson et al., 2013; Zhang et al., 2019). The Love wave phase speed map at 40 s resembles the pattern of the Rayleigh wave phase speed at 30 s in Figure 5b because they have similar depth sensitivities. The low phase speed anomalies in Arctic Alaska and parts of southern Alaska may reveal the influence of a thicker crust, but an imprint of thick sediments also remains in some places. The high phase speed anomaly in the northeastern corner of the map is caused by the North American craton.

At 60 s period (Figure 7c), we use only earthquake data. The Love wave phase speed is primarily sensitive to crustal thickness and uppermost mantle shear wave speeds. North of the Brooks Range, we observe high-phase-speed anomalies extending from west to east, which feature Arctic Alaska and the North American craton in the uppermost mantle. In central Alaska, south of the Tintina fault, north of the Denali fault, a high-speed anomaly region stands out, which is not shown in the Rayleigh wave phase speed maps. This might be related to high radial anisotropy in this region. More results are shown in Figure S11 in Supporting Information S1. The Love wave isotropic phase speed uncertainties are shown in Figure S12 in Supporting Information S1.

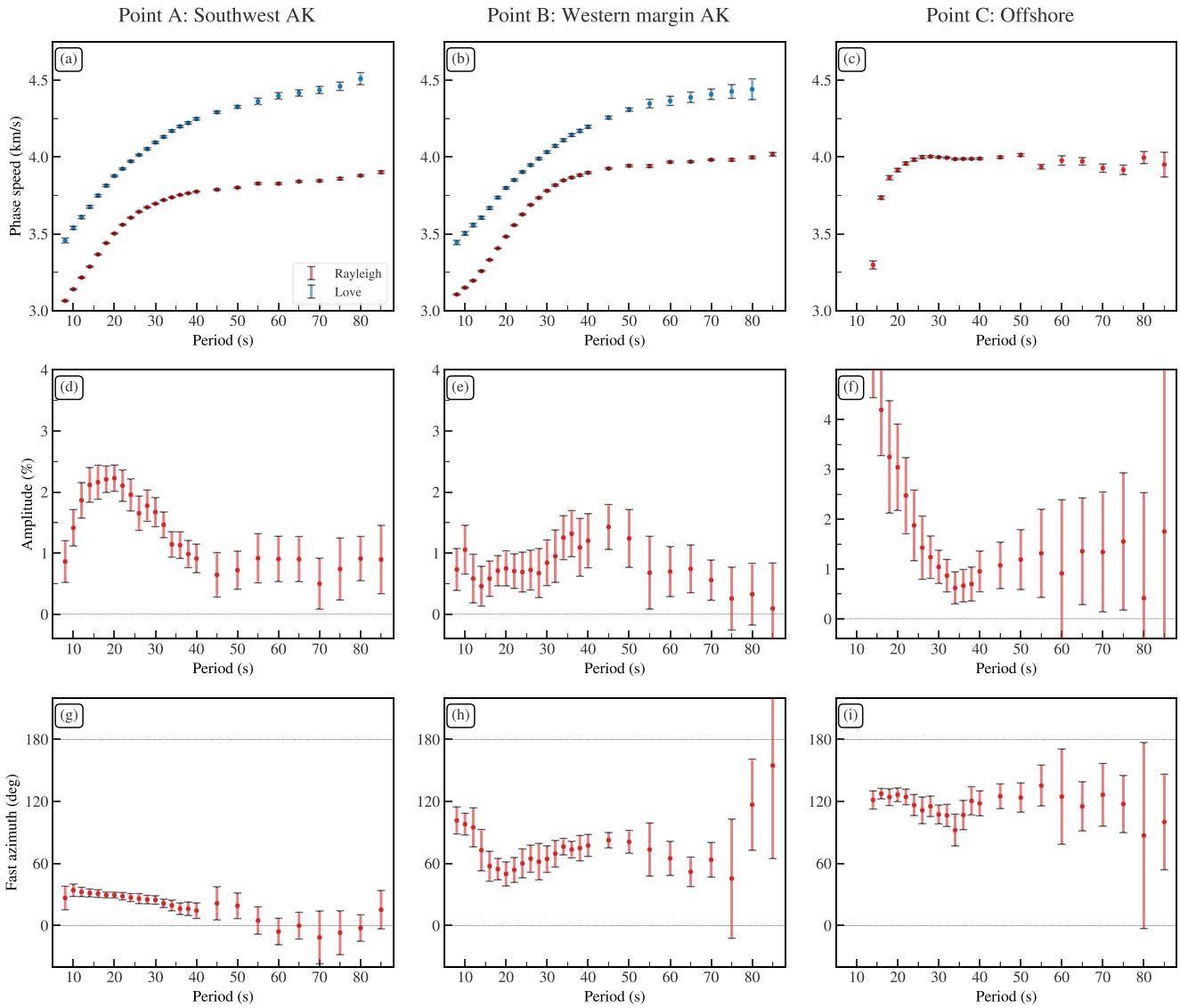

Figure 8. Examples of Rayleigh and Love wave local dispersion curves at three locations: Points A, B, and C identified in Figures 1a–1c Rayleigh (red) and Love (blue) wave isotropic phase speeds. (d–f) The peak-to-peak amplitude ($\boldsymbol{A}_2$) of Rayleigh wave phase speed azimuthal anisotropy. (g–i) Fast azimuth of Rayleigh wave phase speed azimuthal anisotropy in which azimuth is defined clockwise from north. Error bars denote mean ± one standard deviation.

4.5. Local Dispersion Curves for Composite Measurements

Examples of composite isotropic and anisotropic observations from three different locations are shown in Figure 8. Point A is in southwest onshore Alaska, where we have both Rayleigh and Love wave measurements (Figure 8a). Fast axis directions slightly decrease with periods (Figure 8g), which may indicate the relatively coherent vertical deformation at this location from the crust to the uppermost mantle.

Point B is at the western margin of central Alaska. The discrepancy between Love and Rayleigh waves phase speeds is smaller than at point A (Figure 8b), reflecting the relatively weaker radial anisotropy at this location. The fast directions at short periods (8∼14 s) are approximately parallel to the strike orientation of the nearby large right-lateral strike-slip Tintina fault but change gradually as periods increase (Figure 8h). This corresponds to an increase in amplitude at intermediate periods (Figure 8e), which may indicate either a change in the dominant cause of anisotropy or non-coherent vertical deformation between the crust and uppermost mantle.

Point C is offshore Alaska near the trench. We have only Rayleigh wave measurements at this point. Rayleigh wave phase speeds show a sharp increase at short periods (Figure 8c), reflecting the transition from the low-velocity sedimentary layer and sensitivity to the water layer to the high-velocity oceanic crust. The amplitude of Rayleigh wave azimuthal anisotropy is very large at short periods but with considerable uncertainty but then decreases quickly with periods. Fast axes are predominantly trench perpendicular (NW-SE) and relatively stable over periods.

These composite results compiled on a grid across Alaska and offshore constitute our final data set of surface wave observations, including Rayleigh wave isotropic phase speed and azimuthal anisotropy for both onshore and offshore regions and Love wave isotropic phase speeds onshore. This data set is a basis for inferring a depth-dependent 3-D anisotropic model. The observations we present of Rayleigh wave azimuthal anisotropy can be used to construct a depth-dependent azimuthally anisotropic model (e.g., Feng et al., 2020; Lin et al., 2011). Similarly, isotropic Rayleigh and Love wave phase speeds can be used to resolve radial anisotropy (e.g., Feng & Ritzwoller, 2019; Xie et al., 2013). However, the composite measurement is designed to be used together to construct a tilted hexagonally symmetric model of anisotropy by simultaneously interpreting Love and Rayleigh wave isotropic phase speeds and Rayleigh wave azimuthal anisotropy (e.g., Xie et al., 2015, 2017). We present this tilted hexagonally symmetric model in a future contribution.

5. Discussion

5.1. Comparison Between Different Methods

Combining measurements from different methods offer several benefits, including broadening the period range, reducing both random and systematic uncertainties, introducing complementary azimuthal coverage, and providing greater confidence in the final composite results. To determine whether the measurements from the four different methods we consider here can be combined, we need to compare the difference between the results from each method of them. This quantitative comparison also validates the accuracy of the uncertainty estimates. These comparisons form the basis for our decision to use all measurements from the various methods simultaneously.

5.1.1. Qualitative Comparisons

To provide a qualitative impression of the similarity between the different methods, we present examples of maps of isotropic phase speed and the anisotropic quantities (A_2 and ψ_2) constructed using four different methods at specific periods in Figure 9, Figures S13 and S14 in Supporting Information S1. Examples of Rayleigh wave isotropic phase speed at 30 s period are shown in Figure 9. The maps share qualitatively similar first-order features, both onshore and offshore. Figure S13 in Supporting Information S1 shows examples of Rayleigh wave azimuthal anisotropy maps at 30 s periods for both the amplitude and fast axis direction. The general patterns of fast axis directions and amplitudes from the different methods resemble each other qualitatively, such as the roughly fault strike parallel fast directions with relatively strong amplitudes north of the Denali fault. Figure S14 in Supporting Information S1 shows examples of the isotropic Love wave phase speed maps at 40 s period. More quantitative comparisons are presented in Appendix A.

A comparison of the results from different methods and the composite results at three different locations for the 30 s Rayleigh wave is shown in Figure 4. Point A in southwest onshore Alaska has good azimuthal coverage for both ambient noise-based data and earthquake data, and all types of data show relatively consistent azimuthal anisotropy estimates (Figures 4a–4d). Earthquake data tend to have large error bars at azimuths for southward-traveling waves (azimuths near 0° and 360°) because of the paucity of earthquakes north of the study region (Figure 1c). For Point B, near the western margin of central Alaska, the observations from both I_2 and I_3^{ell} cannot provide reliable constraints in the azimuth range of 0°–140° (Figures 4f and 4g) due to the limitation of stations in these directions. Introducing I_3^{hyp} and earthquake data provide complementary azimuthal coverage. Different types of measurements individually do not have complete azimuthal coverage at offshore Point C (Figures 4k–4n). Ambient noise-based data have an azimuthal gap from 90° to 240° (Figures 4k–4m) because of the lack of OBS stations toward the south. However, earthquake data provide complementary observations from earthquakes south of the study area (Figure 4m). Thus, the composite data display more complete azimuthal coverage and offer more reliable azimuthal anisotropy estimates (Figure 4o).

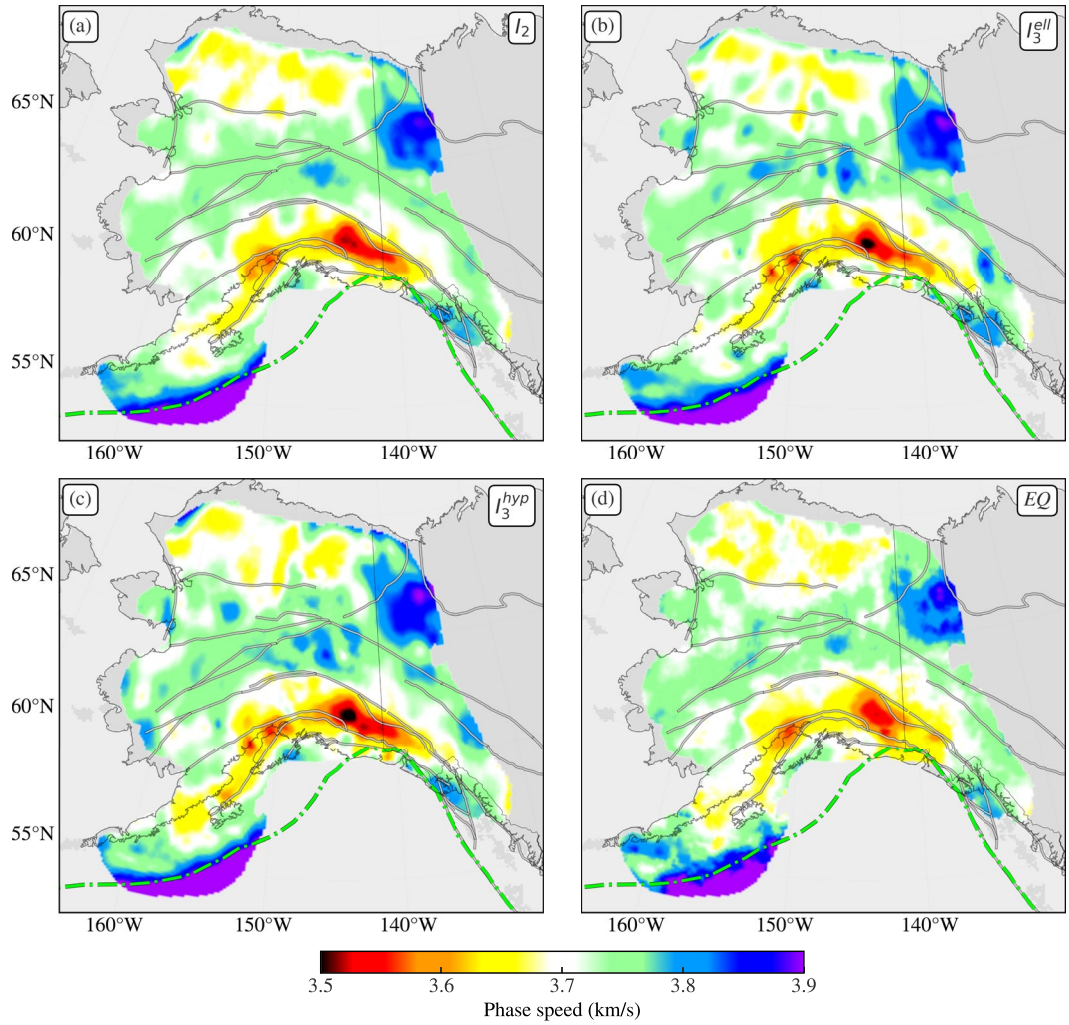

Figure 9. Examples of Rayleigh wave isotropic phase speed maps at 30 s periods from different methods: (a) I_2, (b) I_3^{ell}, (c) I_3^{hyp}, and (d) earthquake data. The lines shown are defined in Figure 6 caption.

5.1.2. Statistical Comparison

To compare the maps from different methods quantitatively, we calculate the spatial mean and standard deviation of the difference between each pair of maps using different methods at the same period. The whole analysis process is presented in Appendix A. In summary, by comparing the results from the different methods, we find that the systematic bias between the methods is small enough so that measurements from different methods can be combined (e.g., Figure 8). This conclusion is based on the observation that the spatial mean of normalized differences is smaller than the threshold value of 1 using the rescaled standard deviations of the variables, on average. Furthermore, the spatial standard deviation of the normalized difference between maps from different methods is close to 1 after upscaling (Section 3.3), consistent with the conclusion that the upscaled uncertainty estimates are accurate. Examples of uncertainty maps for Rayleigh and Love wave isotropic phase speed and Rayleigh azimuthal anisotropy are shown in Figure 10.

5.2. Azimuthal Anisotropy Near the Alaska-Aleutian Subduction Zone

Our discussion here focused on the azimuthally anisotropic patterns beneath the Alaska-Aleutian subduction zone. A 3-D model of shear wave azimuthal anisotropy should be constructed to analyze the depth-dependent anisotropic patterns quantitatively, which we will produce in a future contribution. Here, however, we discuss

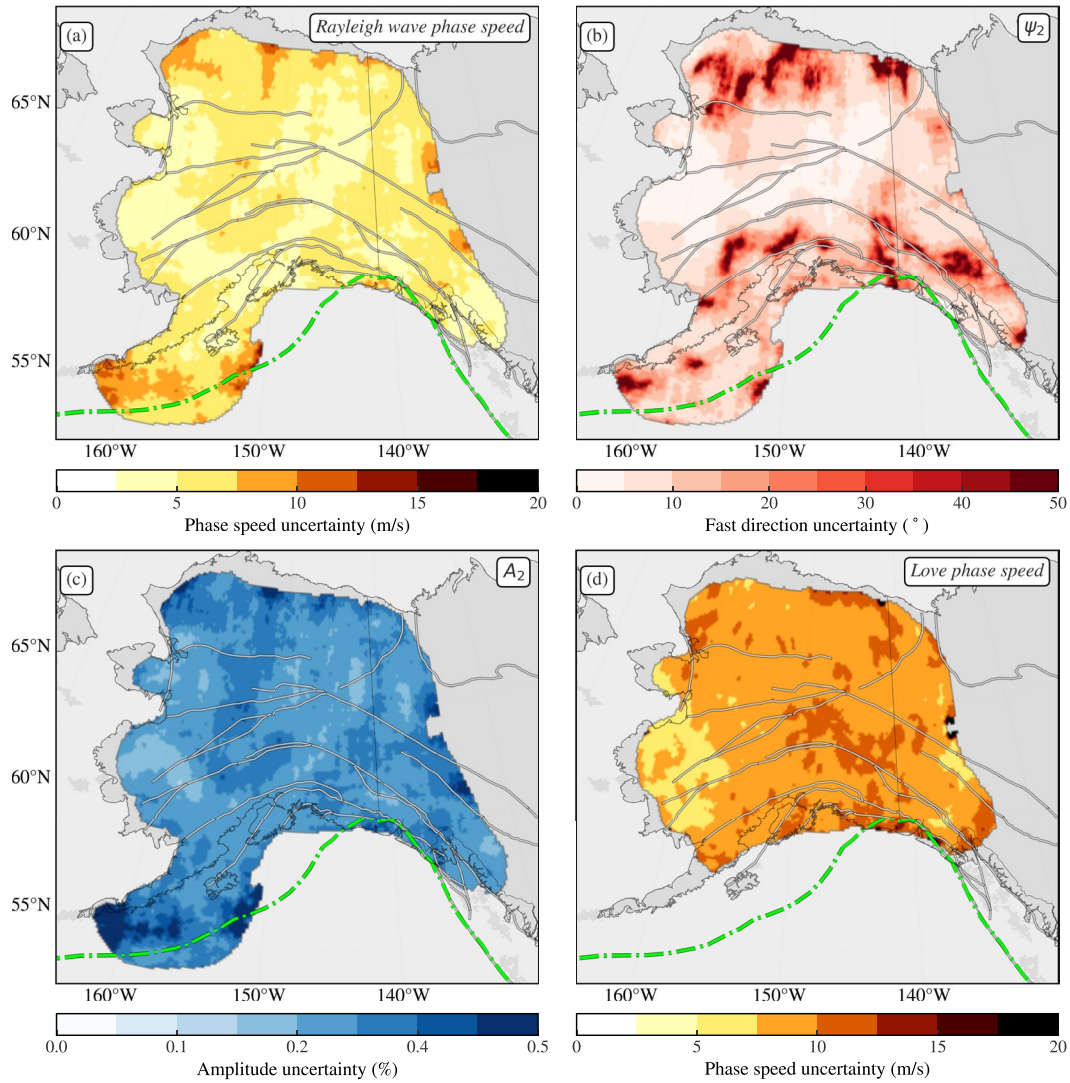

Figure 10. Example uncertainty maps at 40 s period for (a) Rayleigh wave phase speed, (b) fast direction of Rayleigh wave phase speed azimuthal anisotropy, (c) amplitude of Rayleigh wave phase speed azimuthal anisotropy, and (d) Love wave phase speed.

qualitatively the azimuthal anisotropy noting that the longer periods are more sensitive to greater depths. We also compare our anisotropic observations with earlier studies from surface waves, Pn, and shear-wave splitting.

At 20 s period (Figure 11a), the Rayleigh wave phase speed is primarily sensitive to crustal structure onshore and to the accretionary prism and forearc mantle offshore. The region under the influence of subduction is indicated by the slow phase speed anomalies in the accretionary wedge offshore. Fast directions show trench-parallel patterns in both the onshore region and offshore fore-arc region. The phase speed azimuthal anisotropy at this period offshore is comparable to the Pn anisotropy result (He & Lü, 2021). Indeed, Pn tomography also observes the widespread trench-subparallel fast directions in the forearc region (Figure 11a). However, the Pn anisotropy has much smaller amplitudes onshore than offshore, which is not consistent with our result.

At longer periods, 30 and 50 s (Figures 11b and 11c), which are sensitive to deeper structures, the Rayleigh wave azimuthal anisotropy mainly reflects the properties near the bottom of the crust and in the uppermost mantle onshore, and the forearc mantle wedge and uppermost slab offshore. In contrast with the sub-trench-parallel fast direction pattern at 18 s period, the fast directions turn to the sub-trench-perpendicular in most of the forearc region at 30 s period. At 50 s period (Figure 11c), we observe trench-perpendicular fast axis directions in the fore-arc region north of 58°N combined with the sub-parallel fast directions in the back-arc region, forming a

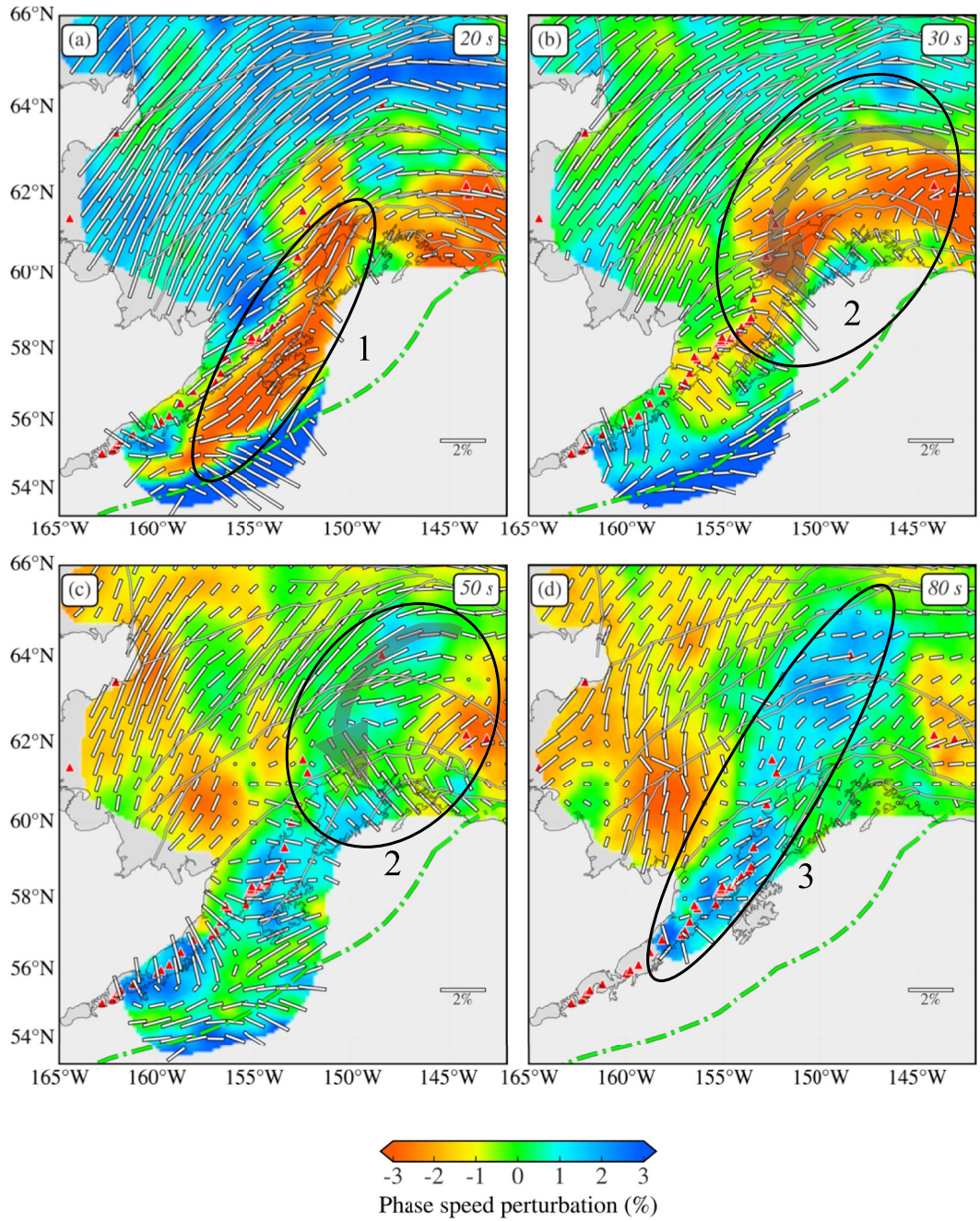

Figure 11. The fast axes for Rayleigh wave phase speed azimuthal anisotropy at periods of (a) 20, (b) 30, (c) 50, and (d) 80 s near the subduction zone. The white bars indicate the fast directions of ψ_2 and the lengths are proportional to the amplitude A_2. The background map shows the phase speed perturbation relative to the mean across the whole region of this study. The red triangles denote volcanoes. The ovals with annotated numbers indicate the noteworthy anisotropic patterns, 1: the trench-parallel pattern in the accretionary prism, 2: horizontally circular pattern in the fore-arc region, as indicated by the overlaying gray arrows; and 3: the trench-parallel pattern within the slab, (see Section 5.2 for details).

horizontally circular pattern. This pattern of fast directions is also shown in the mantle layer of the continental depth-dependent azimuthal anisotropy model of Feng et al. (2020), which used only onshore Rayleigh wave phase speeds. They explained this pattern by invoking toroidal mantle flow around the Alaskan slab edge, which is also predicted by geodynamic modeling (Jadamec & Billen, 2010). However, we also find the fast azimuth gradually

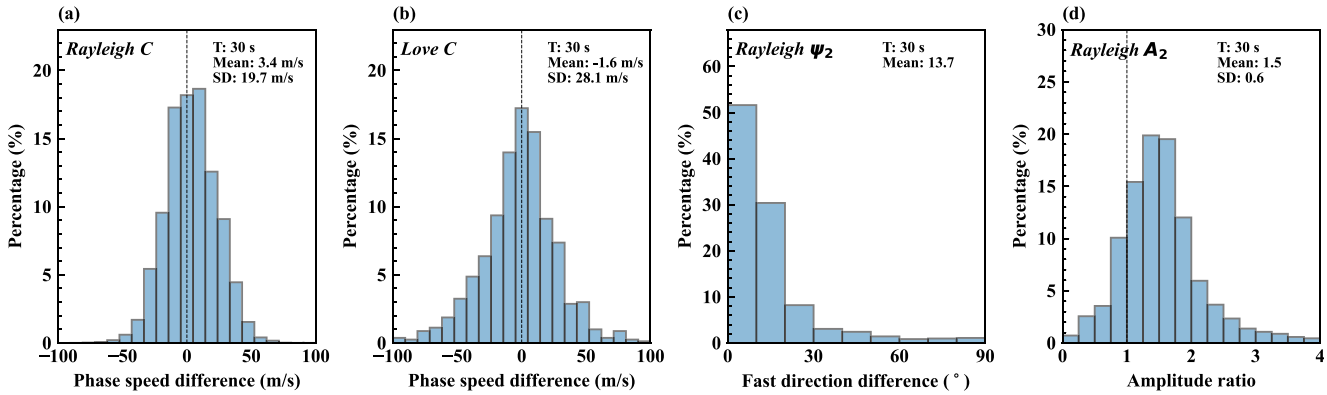

Figure 12. Histograms of the spatial difference between our maps and those of Feng and Ritzwoller (2019) and Feng et al. (2020) at the period of 30 s (a) The Rayleigh wave isotropic phase speed, (b) Love wave isotropic phase speed, (c) fast direction of Rayleigh wave phase speed azimuthal anisotropy, and (d) ratio of the amplitude of azimuthal anisotropy with our result in the numerator and Feng's data set in the denominator.

tends to be trench-parallel in the southern offshore fore-arc area near the trench (south of 58°N), which may reflect the properties of the uppermost subducted slab.

Going to even longer periods, at 80 s (Figure 11d), the subducted slab is well identified by high isotropic speeds. The fast directions in this region mainly reflect the upper structure of the slab. We observe clear approximately trench-parallel fast directions within the slab, which is consistent with SKS measurements (e.g., Venereau et al., 2019). These trench-parallel fast directions are probably caused by trench-parallel structural fabrics within the subducted slab, which might be acquired before subduction.

In summary, in the region of the subduction zone, we observe trench-parallel fast directions in the accretionary wedge at shallow depth, a trench-perpendicular pattern in the forearc mantle wedge, and trench-parallel fast directions within the uppermost slab. For the offshore region, Lynner (2021) observed trench-parallel SKS fast directions in the Shumagin seismic gap and the Kodiak Segment, while trench-perpendicular splitting was found in the Semidi Segment. They suggested this variation may be caused by different hydration of the slab along the subduction zone, which may result in different megathrust earthquake behavior. Our measurements of azimuthal anisotropy indicate that anisotropy in this tectonic environment may be even more complex. Inversion for a depth-dependent azimuthally anisotropic model will be the subject of a future contribution.

5.3. Comparison With Previous Studies

Here, we compare our Rayleigh and Love wave maps onshore with those from Feng and Ritzwoller (2019) and Feng et al. (2020), which we refer to as Feng's maps. Feng's maps are based on the traditional two-station ambient noise interferometry and earthquake tomography using seismic records at onshore stations. Our data set differs from theirs in the introduction of observations from OBS stations (AACSE), using of seismic records accumulated over a longer time period, applying three-station interferometry for ambient noise data and Helmholtz tomography for earthquake data rather than eikonal tomography.

To analyze the difference quantitatively between our new dispersion maps and Feng's maps, we calculate the spatial mean and standard deviation of the difference between the two maps for the isotropic Rayleigh and Love wave phase speed and the fast azimuth directions. For the amplitude of azimuthal anisotropy, instead of computing the difference, we use the ratio where our result is in the numerator and Feng's in the denominator. The results at 30 s period are shown in Figure 12 and results at other periods are shown in Figure S15 in Supporting Information S1.

The spatial mean of the difference between the two maps onshore for Rayleigh and Love wave isotropic phase speeds is on the order of only a few meters per second (Figures 12a and 12b, Figures S15a–S15c, and S15j–S15l in Supporting Information S1). Even though the spatial mean difference between the maps is small, the visual differences are significant: for example, our new maps depict a clearer subduction zone with a high-speed anomaly at long periods (Figure 13). We also calculate the unitless spatial mean of the normalized difference between

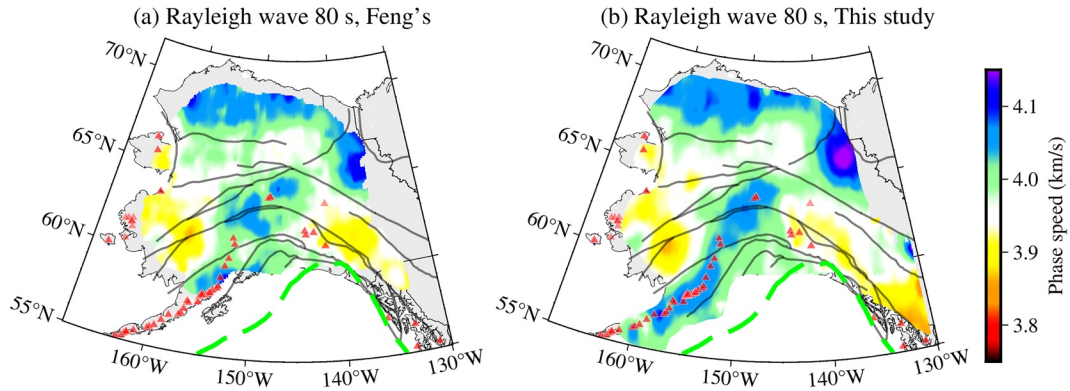

Figure 13. Rayleigh wave isotropic phase speed maps at 80 s period from (a) Feng et al. (2020) and (b) this study. The red triangles denote volcanoes.

two data sets at different periods, as we mentioned in Section 5.1.2. These results are near zero, indicating little systematic difference between maps. For the fast directions of azimuthal anisotropy, the majority of locations have an orientation difference within 10° (Figure 12d).

The most significant difference lies in the amplitude of azimuthal anisotropy between the two sets of maps. On average, the amplitude ratio is around 1.5 (Figure 12c), which indicates that our amplitudes of azimuthal anisotropy are typically about 50% larger than those of Feng's at nearly all periods. This is consistent with their conclusion of the systematic underestimation of amplitude by 50% (Feng et al., 2020) caused by a large smoothing radius of 200 km, in contrast to the average radius of about 130 km that we apply (Section 3). This choice of smoothing radius in the estimation of azimuthal anisotropy is ad hoc. The large smoothing radius reduces the variation in measurements but also reduces the amplitude and resolution of anisotropy. Also, in contrast with Feng's study, we use three-station ambient noise interferometry, which substantially increases the number of the measurements and improves azimuthal coverage. We also apply Helmholtz tomography for earthquake data to correct for finite frequency effects. These factors combined with a larger data set give us the confidence to use the smaller smoothing radius.

Another difference with respect to the study of Feng and Ritzwoller (2019) and Feng et al. (2020) is that we extend the longest period for the Love wave isotropic phase speeds from 50 to 80 s. By using Helmholtz tomography and longer seismic records for earthquake data, the longer period Love wave data may help to constrain the deeper radial anisotropic structure of the uppermost mantle beneath Alaska.

In summary, our continental data set is consistent with Feng's data set at most locations for isotropic Rayleigh and Love wave phase speed and fast azimuth directions. Our amplitude measurements, however, are about 50% larger than Feng's. Their underestimation of the amplitude of azimuthal anisotropy is caused by their choice of a larger smoothing radius in the estimation of azimuthal anisotropy, which they acknowledged in their paper.

6. Conclusion

We use seismic observations both onshore and offshore Alaska to construct a surface wave dispersion database, including Rayleigh wave isotropic phase speed and azimuthal anisotropy at periods from 8 to 85 s and Love wave isotropic phase speed at periods from 8 to 80 s. We use three methods to produce surface wave measurements, including two-station and three-station ambient noise interferometry with eikonal tomography and Helmholtz tomography for earthquake data. Compared with traditional two-station ambient noise interferometry, three-station interferometry yields a significantly improved SNR and an increase in the number of measurements for both Rayleigh and Love waves by more than 50% (Section 2.3).

We find that the systematic bias between methods is small enough (less than 1 joint uncertainty on average) so that the measurements can be combined to produce a single combined data set (Section 5.1). Compared with using a single method, combining measurements from different methods into a composite database offers several benefits, including broadening the period range of the measurements, reducing both random and systematic

uncertainties, introducing complementary azimuthal coverage, and providing greater confidence in the final composite results.

The composite results we present provide nearly complete coverage onshore Alaska and in select regions offshore of Alaska. Both Rayleigh and Love wave isotropic phase speed maps and azimuthal anisotropy are geologically understandable and stand in a reasonable relation to known geological structures (Section 4). The data set onshore is consistent with previous studies of isotropic phase speeds and the fast direction of azimuthal anisotropy (Feng & Ritzwoller, 2019; Feng et al., 2020), but our results provide more reliable amplitude estimates for azimuthal anisotropy at all periods (Section 5.3).

With data from the OBS stations (AACSE), we extend the Rayleigh wave isotropic and anisotropic maps offshore, which produces significantly better coverage in the Alaska-Aleutian subduction zone. Near the subduction zone, we observe trench-parallel fast directions in the accretionary wedge at shallow depths, a trench-perpendicular pattern in the forearc mantle wedge, and trench-parallel fast directions within the uppermost slab (Section 5.2). The pattern of azimuthal anisotropy reflects the complicated tectonic and geodynamic environment in this region.

The final product of the surface wave dispersion data set provides a basis for inferring depth-dependent 3-D isotropic and anisotropic models. The isotropic Rayleigh wave phase speed can be used in a joint inversion with receiver functions and Rayleigh wave ellipticity (e.g., Shen & Ritzwoller, 2016 in West US, Berg et al., 2020 in Alaska). The Rayleigh wave azimuthal anisotropy complements shear wave splitting measurements both onshore (e.g., Venereau et al., 2019) and offshore (e.g., Lynner, 2021) and may be used to construct a depth-dependent azimuthally anisotropic model (e.g., Feng et al., 2020; Lin et al., 2011). The isotropic Rayleigh and Love wave phase speeds can be used to resolve radial anisotropy (e.g., Feng & Ritzwoller, 2019). In a future contribution, we plan to use the composite measurements to construct a tilted hexagonally symmetric model of anisotropy by simultaneously interpreting Love and Rayleigh wave isotropic phase speeds and Rayleigh wave azimuthal anisotropy as was done by Xie et al. (2015, 2017). The resolved depth-dependent elastic tensors will help to explore the geometry of anisotropy and to investigate the corresponding deformation in the crust and uppermost mantle beneath Alaska. This tilted transverse isotropic model will provide a more complete and consistent explanation of the anisotropy of Alaska.

Appendix A: Statistic Comparison Between Different Methods

To compare the maps from different methods quantitatively, we calculate the spatial mean and standard deviation of the difference between each pair of maps using different methods at the same period. Examples of maps and histograms of the difference for each quantity are shown in Figures S16 and S17 in Supporting Information S1, respectively. To evaluate the systematic bias and the adequacy of our uncertainty estimates, we construct the spatial mean and standard deviation of the normalized difference between maps using the joint uncertainty in terms of Welch's unequal variance t-test (e.g., Zhang et al., 2021). The joint uncertainty of any quantity in the comparison between two maps from method A and method B at location $\boldsymbol{r}$ is:

$$\sigma_{A,B}(\boldsymbol{r}) = \sqrt{\sigma_A^2(\boldsymbol{r}) + \sigma_B^2(\boldsymbol{r})}. \tag{A1}$$

The spatial mean joint uncertainty curves for different quantities as a function of the period are shown in Figure S18 in Supporting Information S1. We use the unitless spatial mean of the normalized difference between two maps as an estimate of the systematic bias between the maps. The results should be near 1, unless there is a systematic error. Typically, results are less than one. When it is larger than 1, this may mean that the uncertainties are underestimated for either or both maps; however, when it is smaller than 1, we may have overestimated the uncertainties.

Figure A1 shows the spatial mean difference (including units) between each I_2 map and those from other methods for isotropic phase speed and the anisotropic quantities (A_2 and ψ_2) over period. Figures S19 and S20 in Supporting Information S1 show the unitless spatial mean and standard deviation of the normalized difference, respectively.

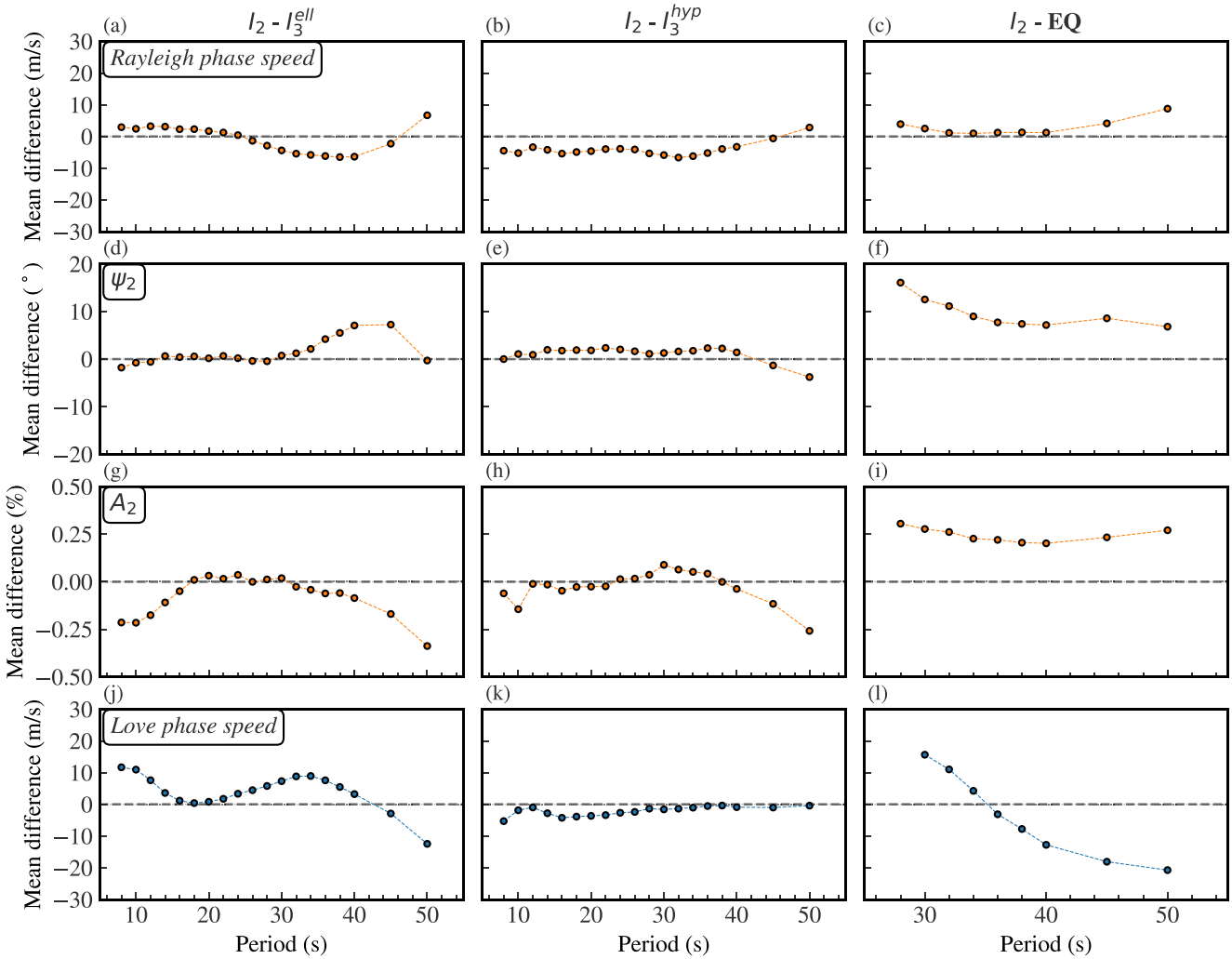

Figure A1. Spatial means of the period-dependent difference between Rayleigh and Love wave isotropic and anisotropic maps from different methods. (a–c) The Rayleigh wave isotropic phase speed. (d–f) The fast direction of Rayleigh wave phase speed azimuthal anisotropy. (g–i) The amplitude of Rayleigh wave phase speed azimuthal anisotropy. (j–l) The Love wave isotropic phase speed.

For Rayleigh wave isotropic phase speed, Figures A1a–A1c shows the Rayleigh wave isotropic phase speed spatial mean of differences between pairs of maps from I_2 and one of I_3^{ell}, I_3^{hyp}, and earthquake data, respectively. These spatial mean difference values are smaller than 20 m/s in the periods of overlap between the methods. At short periods (<30 s), I_3^{ell} is slightly slower than I_2 in contrast with I_3^{hyp}, which is faster than I_2. In the period range of overlap between the methods, we find that the I_2 maps are slightly systemically faster than earthquake maps. It has been reported elsewhere that the effect reduces with an increase in the number of earthquake measurements (Shen & Ritzwoller, 2016). The spatial mean of the normalized difference is less than 1 for all the comparisons (Figures S19a–S19c in Supporting Information S1), which implies only a low level of systematic bias and establishes the consistency between the different methods.

The spatial average joint uncertainty between I_2 and three-station interferometry (I_3^{ell} and I_3^{hyp}) minimizes around 20 s period, and the joint uncertainties between I_2 and earthquake maps minimize around 40 s period (Figures S18a–S18c in Supporting Information S1). Joint uncertainty values predominantly reflect data quality including the SNR and the number of measurements (Figures 3a and 3c). Figures S20a–S20c in Supporting Information S1 shows that the unitless spatial standard deviation of the normalized difference before the additional upscaling is around 1.6 in the comparison between I_2 and I_3^{ell}, I_3^{hyp}. For I_2 and earthquake maps, it is around 1.3 before additional upscaling. These values are larger than the threshold value of 1. These results indicate that it may be

best to upscale uncertainty by an additional factor of about 1.4 over and above the upscaling based on misfit, which is described in Section 3.3. After applying an extra upscaling by a factor of 1.4, the unitless spatial standard deviations are close to 1 in all the comparisons (Figures S20a–S20c in Supporting Information S1).

As for the anisotropic quantities, fast axis direction and amplitude, Figures A1d–A1i shows the spatial mean of their differences taken over the maps. The fast directions from ambient noise (I_2 and I_3^{ell}, I_3^{hyp}) are more similar to each other, with an average angle difference around 1° (Figures A1d and A1e), than they are to earthquake data, with an average angle difference of around 10° (Figure A1c). As for the amplitude, I_2 is consistent with I_3^{ell} and I_3^{hyp} in most of the period range except for the shortest and longest periods (Figures 10g and 10h). This is primarily due to fewer measurements and poorer azimuthal coverage in the shortest and longest period bands. The amplitude of anisotropy in the I_2 maps is systematically larger than in the earthquake maps by ∼0.23% on average (Figure 10i). This systemic bias may be caused by the spatially larger sensitivity kernel for earthquake measurements given the longer earthquake paths than the inter-station paths of I_2. Overall, the spatial mean of the difference between I_2 and other methods is smaller than one times the average joint uncertainty across all periods (Figures S19d–S19i in Supporting Information S1), which confirms the consistency between different methods. Figures S20d–S20i in Supporting Information S1 confirms the accuracy of the uncertainty estimates for both fast direction and amplitude of azimuthal anisotropy, because the spatial standard deviation of the normalized difference curves is close to one in all comparisons.

Figures A1j–A1l show the spatial mean value curves of the difference between pairs of maps for different methods for Love wave isotropic phase speed. In contrast with the comparison between I_2 and I_3^{hyp}, the discrepancy between I_2 and I_3^{ell} is more variable and the differences are larger, which probably reflects the fewer number of measurements for I_3^{ell} than for I_3^{hyp} (Figure 3c). We find that I_2 Love wave phase speeds are systematically faster than those from earthquakes from 30 to 36 s period, then they are slower than from earthquakes at longer periods (Figure 10l). Systematically faster I_2 Rayleigh wave phase speeds are found both in Alaska (Figure A1c) and in Cascadia (Zhang et al., 2021). But a systematically faster earthquake phase speed has been reported earlier elsewhere and may be more common (e.g., Yang et al., 2008; Yao et al., 2006). Such discrepancies are not well understood but are perhaps due to different sensitivities of earthquake data and ambient noise data to lateral heterogeneities (Kästle et al., 2016). Even though the systematic bias for the Love wave phase speed is larger than that for Rayleigh waves, the spatial mean of the normalized difference is still smaller than the threshold value (<1) to be considered systematically different (Figures S19j–S19l in Supporting Information S1). The corresponding spatial standard deviation of the normalized difference between maps (Figures S20j–S20l in Supporting Information S1) indicates that the uncertainties are underestimated by a factor of 3 for all methods before upscaling. After applying upscale (Section 3.3), the unitless spatial standard deviations of the normalized difference are close to 1.

Acknowledgments
We thank the associate editor and the reviewers, Carl Tape and anonymous, for constructive comments that helped to improve this paper. We are grateful to Lili Feng and Mengyu Wu for providing helpful suggestions. We greatly appreciate the community members that contributed to the data acquisition of the Alaska Transportable Array, Alaska Regional Network, AACSE, and other permanent and temporary networks in the region. We could not have conducted this study without their contributions. We thank the researchers and institutions involved with collecting these valuable data. The facilities of IRIS Data Services, and specifically the IRIS Data Management Center, were used for access to waveforms, related metadata and/or derived products used in this study. IRIS Data Services are funded through the Seismological Facilities for the Advancement of Geoscience and EarthScope (SAGE) Proposal of the National Science Foundation (NSF) under Cooperative Agreement EAR-1851048. This study was funded by NSF Grants EAR-1537868, EAR-1928395, and EAR-1952209 at the University of Colorado Boulder.

Data Availability Statement

The network codes for seismic data used in this study include 5C, 7C, 9C, AK, AT, AV, CN, GM, II, IM, IU, PN, PO, PP, TA, US, XE, XF, XI, XN, XO, XR, XV, XY, Y2, YE, YG, YM, YV, Z5, ZE, and ZQ. DOIs for these networks can be found in Table S1 in Supporting Information S1. The composite surface wave dispersion maps and stacked three-station interferograms are available on Zenodo (Liu et al., 2022, https://doi.org/10.5281/zenodo.7080282). The source code of ambient noise three-station interferometry is available on GitHub (https://github.com/NoiseCIEI/ThreeStation). Some figures were made using Generic Mapping Tools (GMT) version 6 (Wessel et al., 2019) licensed under LGPL. Other figures were made with Matplotlib version 3.2.1 (Caswell et al., 2020; Hunter, 2007).

References

Barcheck, G., Abers, G. A., Adams, A. N., Bécel, A., Collins, J., Gaherty, J. B., et al. (2020). The Alaska amphibious community seismic experiment. *Seismological Research Letters*, *91*(6), 3054–3063. https://doi.org/10.1785/0220200189

Barmin, M. P., Ritzwoller, M. H., & Levshin, A. L. (2001). A fast and reliable method for surface wave tomography. *Pure and Applied Geophysics*, *158*(8), 1351–1375. https://doi.org/10.1007/pl00001225

Bell, S. W., Forsyth, D. W., & Ruan, Y. (2015). Removing noise from the vertical component records of ocean-bottom seismometers: Results from year one of the Cascadia Initiative. *Bulletin of the Seismological Society of America*, *105*(1), 300–313. https://doi.org/10.1785/0120140054

Bensen, G. D., Ritzwoller, M. H., Barmin, M. P., Levshin, A. L., Lin, F., Moschetti, M. P., et al. (2007). Processing seismic ambient noise data to obtain reliable broad-band surface wave dispersion measurements. *Geophysical Journal International*, *169*(3), 1239–1260. https://doi.org/10.1111/j.1365-246x.2007.03374.x

Berg, E. M., Lin, F., Allam, A., Schulte-Pelkum, V., Ward, K. M., & Shen, W. (2020). Shear velocity model of Alaska via joint inversion of Rayleigh wave ellipticity, phase velocities, and receiver functions across the Alaska transportable Array. *Journal of Geophysical Research: Solid Earth*, *125*(2), e2019JB018582. https://doi.org/10.1029/2019jb018582

Busby, R. W., & Aderhold, K. (2020). The Alaska transportable Array: As built. *Seismological Research Letters*, *91*(6), 3017–3027. https://doi.org/10.1785/0220200154

Caswell, T., Droettboom, M., Lee, A., Hunter, J., Firing, E., Stansby, D., et al. (2020). Matplotlib v3.2.1 [Dataset]. Zenodo. https://doi.org/10.5281/zenodo.3714460

Chen, Y., & Saygin, E. (2020). Empirical Green's function retrieval using ambient noise source-receiver interferometry. *Journal of Geophysical Research: Solid Earth*, *125*(2), e2019JB018261. https://doi.org/10.1029/2019jb018261

Christeson, G. L., Van Avendonk, H. J. A., Gulick, S. P. S., Reece, R. S., Pavlis, G. L., & Pavlis, T. L. (2013). Moho interface beneath Yakutat terrane, southern Alaska. *Journal of Geophysical Research: Solid Earth*, *118*(9), 5084–5097. https://doi.org/10.1002/jgrb.50361

Colpron, M., Nelson, J. L., & Murphy, D. C. (2007). Northern Cordilleran terranes and their interactions through time. *Geological Society of America Today*, *17*(4), 4. https://doi.org/10.1130/gsat01704-5a.1

Crampin, S. (1984). Effective anisotropic elastic constants for wave propagation through cracked solids. *Geophysical Journal International*, *76*(1), 135–145. https://doi.org/10.1111/j.1365-246x.1984.tb05029.x

Crawford, W. C., & Webb, S. C. (2000). Identifying and removing tilt noise from low-frequency (<0.1 Hz) seafloor vertical seismic data. *Bulletin of the Seismological Society of America*, *90*(4), 952–963. https://doi.org/10.1785/0119990121

Curtis, A., Behr, Y., Entwistle, E., Galetti, E., Townend, J., & Bannister, S. (2012). The benefit of hindsight in observational science: Retrospective seismological observations. *Earth and Planetary Science Letters*, *345*, 212–220. https://doi.org/10.1016/j.epsl.2012.06.008

Curtis, A., & Halliday, D. (2010). Source-receiver wave field interferometry. *Physical Review E*, *81*(4), 046601. https://doi.org/10.1103/physreve.81.046601

Eberhart-Phillips, D., Christensen, D. H., Brocher, T. M., Hansen, R., Ruppert, N. A., Haeussler, P. J., & Abers, G. A. (2006). Imaging the transition from Aleutian subduction to Yakutat collision in central Alaska, with local earthquakes and active source data. *Journal of Geophysical Research*, *111*(B11), B11303. https://doi.org/10.1029/2005jb004240

Feng, L. (2021). Amphibious shear wave structure beneath the Alaska-Aleutian subduction zone from ambient noise tomography. *Geochemistry, Geophysics, Geosystems*, *22*(5), e2020GC009438. https://doi.org/10.1029/2020gc009438

Feng, L., Liu, C., & Ritzwoller, M. H. (2020). Azimuthal anisotropy of the crust and uppermost mantle beneath Alaska. *Journal of Geophysical Research: Solid Earth*, *125*(12), e2020JB020076. https://doi.org/10.1029/2020jb020076

Feng, L., & Ritzwoller, M. H. (2019). A 3-D shear velocity model of the crust and uppermost mantle beneath Alaska including apparent radial anisotropy. *Journal of Geophysical Research: Solid Earth*, *124*(10), 10468–10497. https://doi.org/10.1029/2019jb018122

Fuis, G. S., Moore, T. E., Plafker, G., Brocher, T. M., Fisher, M. A., Mooney, W. D., et al. (2008). Trans-Alaska Crustal Transect and continental evolution involving subduction underplating and synchronous foreland thrusting. *Geology*, *36*(3), 267–270. https://doi.org/10.1130/g24257a.1

Gama, I., Fischer, K. M., Eilon, Z., Krueger, H. E., Dalton, C. A., & Flesch, L. M. (2021). Shear-wave velocity structure beneath Alaska from a Bayesian joint inversion of Sp receiver functions and Rayleigh wave phase velocities. *Earth and Planetary Science Letters*, *560*, 116785. https://doi.org/10.1016/j.epsl.2021.116785

Gou, T., Zhao, D., Huang, Z., & Wang, L. (2019). Aseismic deep slab and mantle flow beneath Alaska: Insight from anisotropic tomography. *Journal of Geophysical Research: Solid Earth*, *124*(2), 1700–1724. https://doi.org/10.1029/2018jb016639

Hayes, G. P., Moore, G. L., Portner, D. E., Hearne, M., Flamme, H., Furtney, M., & Smoczyk, G. M. (2018). Slab2, a comprehensive subduction zone geometry model. *Science*, *362*(6410), 58–61. https://doi.org/10.1126/science.aat4723

He, Y., & Lü, Y. (2021). Anisotropic Pn tomography of Alaska and adjacent regions. *Journal of Geophysical Research: Solid Earth*, *126*(11), e2021JB022220. https://doi.org/10.1029/2021jb022220

Hunter, J. D. (2007). Matplotlib: A 2D graphics environment. *Computing in Science & Engineering*, *9*(3), 90–95. https://doi.org/10.1109/MCSE.2007.55

Jadamec, M. A., & Billen, M. I. (2010). Reconciling surface plate motions with rapid three-dimensional mantle flow around a slab edge. *Nature*, *465*(7296), 338–341. https://doi.org/10.1038/nature09053

Janiszewski, H., Gaherty, J. B., Abers, G. A., Gao, H., & Eilon, Z. C. (2019). Amphibious surface-wave phase-velocity measurements of the Cascadia subduction zone. *Geophysical Journal International*, *217*(3), 1929–1948. https://doi.org/10.1093/gji/ggz051

Jiang, C., Schmandt, B., Ward, K. M., Lin, F., & Worthington, L. L. (2018). Upper mantle seismic structure of Alaska from Rayleigh and S wave tomography. *Geophysical Research Letters*, *45*(19), 10350–10359. https://doi.org/10.1029/2018gl079406

Johnston, S. T. (2001). The great Alaskan terrane wreck: Reconciliation of paleomagnetic and geological data in the northern Cordillera. *Earth and Planetary Science Letters*, *193*(3-4), 259–272. https://doi.org/10.1016/S0012-821X(01)00516-7

Kästle, E. D., Molinari, I., Boschi, L., & Kissling, E. (2021). Azimuthal anisotropy from eikonal tomography: Example from ambient-noise measurements in the AlpArray network. *Geophysical Journal International*, *229*(1), 151–170. https://doi.org/10.1093/gji/ggab453

Kästle, E. D., Soomro, R., Weemstra, C., Boschi, L., & Meier, T. (2016). Two-receiver measurements of phase velocity: Cross-validation of ambient-noise and earthquake-based observations. *Geophysical Journal International*, *207*(3), 1493–1512. https://doi.org/10.1093/gji/ggw341

Lebigot, E. (2022). Uncertainties: A Python package for calculations with uncertainties, (version 3.17) [Dataset]. Retrieved from https://uncertainties-python-package.readthedocs.io/en/latest/

Levshin, A. L., & Ritzwoller, M. H. (2001). Automated detection, extraction, and measurement of regional surface waves (pp. 1531–1545). https://doi.org/10.1007/978-3-0348-8264-4_11

Li, J., Shillington, D. J., Bécel, A., Nedimović, M. R., Webb, S. C., Saffer, D. M., et al. (2015). Downdip variations in seismic reflection character: Implications for fault structure and seismogenic behavior in the Alaska subduction zone. *Journal of Geophysical Research: Solid Earth*, *120*(11), 7883–7904. https://doi.org/10.1002/2015jb012338

Lin, F., Moschetti, M. P., & Ritzwoller, M. H. (2008). Surface wave tomography of the western United States from ambient seismic noise: Rayleigh and Love wave phase velocity maps. *Geophysical Journal International*, *173*(1), 281–298. https://doi.org/10.1111/j.1365-246x.2008.03720.x

Lin, F., & Ritzwoller, M. H. (2011a). Apparent anisotropy in inhomogeneous isotropic media. *Geophysical Journal International*, *186*(3), 1205–1219. https://doi.org/10.1111/j.1365-246x.2011.05100.x

Lin, F., & Ritzwoller, M. H. (2011b). Helmholtz surface wave tomography for isotropic and azimuthally anisotropic structure. *Geophysical Journal International*, *186*(3), 1104–1120. https://doi.org/10.1111/j.1365-246x.2011.05070.x

Lin, F., Ritzwoller, M. H., & Snieder, R. (2009). Eikonal tomography: Surface wave tomography by phase front tracking across a regional broad-band seismic array. *Geophysical Journal International*, *177*(3), 1091–1110. https://doi.org/10.1111/j.1365-246x.2009.04105.x

Lin, F., Ritzwoller, M. H., Yang, Y., Moschetti, M. P., & Fouch, M. J. (2011). Complex and variable crustal and uppermost mantle seismic anisotropy in the western United States. *Nature Geoscience*, *4*(1), 55–61. https://doi.org/10.1038/ngeo1036

Liu, C., Yao, H., Yang, H., Shen, W., Fang, H., Hu, S., & Qiao, L. (2019). Direct inversion for three-dimensional shear wave speed azimuthal anisotropy based on surface wave ray tracing: Methodology and application to Yunnan, southwest China. *Journal of Geophysical Research: Solid Earth*, *124*(11), 11394–11413. https://doi.org/10.1029/2018jb016920

Liu, C., Zhang, S., Sheehan, A. F., & Ritzwoller, M. H. (2022). Surface wave isotropic and azimuthally anisotropic dispersion across Alaska and the Alaska-Aleutian subduction zone [Dataset]. Zenodo. Retrieved from https://doi.org/10.5281/zenodo.7080282

Lynner, C. (2021). Anisotropy-revealed change in hydration along the Alaska subduction zone. *Geology*, *49*(9), 1122–1125. https://doi.org/10.1130/g48860.1

Ma, S., & Beroza, G. C. (2012). Ambient-field Green's functions from asynchronous seismic observations. *Geophysical Research Letters*, *39*(6), L06301. https://doi.org/10.1029/2011gl050755

Mann, M. E., Abers, G. A., Daly, K., & Christensen, D. H. (2021). Subduction of an oceanic plateau across southcentral Alaska: Scattered-wave imaging. *Journal of Geophysical Research: Solid Earth*, *127*(1), e2021JB022697. https://doi.org/10.1029/2021jb022697

Martin-Short, R., Allen, R., Bastow, I. D., Porritt, R. W., & Miller, M. S. (2018). Seismic imaging of the Alaska subduction zone: Implications for slab geometry and volcanism. *Geochemistry, Geophysics, Geosystems*, *19*(11), 4541–4560. https://doi.org/10.1029/2018gc007962

McPherson, A. M., Christensen, D. H., Abers, G. A., & Tape, C. (2020). Shear wave splitting and mantle flow beneath Alaska. *Journal of Geophysical Research: Solid Earth*, *125*(4), e2019JB018329. https://doi.org/10.1029/2019jb018329

Miller, M. S., & Moresi, L. (2018). Mapping the Alaskan Moho. *Seismological Research Letters*, *89*(6), 2430–2436. https://doi.org/10.1785/0220180222

Moore, T. E., & Box, S. E. (2016). Age, distribution, and style of deformation in Alaska north of 60 N: Implications for assembly of Alaska. *Tectonophysics*, *691*, 133–170. https://doi.org/10.1016/j.tecto.2016.06.025

Nayak, A., Eberhart-Phillips, D., Ruppert, N. A., Fang, H., Moore, M. M., Tape, C., et al. (2020). 3D seismic velocity models for Alaska from joint tomographic inversion of body-wave and surface-wave data. *Seismological Research Letters*, *91*(6), 3106–3119. https://doi.org/10.1785/0220200214

Plafker, G., & Berg, H. (1994). Overview of the geology and tectonic evolution of Alaska (pp. 989–1021). https://doi.org/10.1130/dnag-gna-g1.989

Richards, C., Tape, C., Abers, G. A., & Ross, Z. E. (2021). Anisotropy variations in the Alaska subduction zone based on shear-wave splitting from intraslab earthquakes. *Geochemistry, Geophysics, Geosystems*, *22*(5), e2020GC009558. https://doi.org/10.1029/2020gc009558

Sabra, K. G., Gerstoft, P., Roux, P., Kuperman, W. A., & Fehler, M. C. (2005). Surface wave tomography from microseisms in Southern California: Surface wave tomography. *Geophysical Research Letters*, *32*(14), L14311. https://doi.org/10.1029/2005gl023155

Schulte-Pelkum, V., Caine, J. S., Jones, J. V., & Becker, T. W. (2020). Imaging the tectonic grain of the northern Cordillera Orogen using Transportable Array receiver functions. *Seismological Research Letters*, *91*(6), 3086–3105. https://doi.org/10.1785/0220200182

Shapiro, N. M., & Campillo, M. (2004). Emergence of broadband Rayleigh waves from correlations of the ambient seismic noise. *Geophysical Research Letters*, *31*(7), L07614. https://doi.org/10.1029/2004gl019491

Shapiro, N. M., Campillo, M., Stehly, L., & Ritzwoller, M. H. (2005). High-resolution surface-wave tomography from ambient seismic noise. *Science*, *307*(5715), 1615–1618. https://doi.org/10.1126/science.1108339

Shen, W., & Ritzwoller, M. H. (2016). Crustal and uppermost mantle structure beneath the United States. *Journal of Geophysical Research: Solid Earth*, *121*(6), 4306–4342. https://doi.org/10.1002/2016jb012887

Shephard, G. E., Müller, R. D., & Seton, M. (2013). The tectonic evolution of the Arctic since Pangea breakup: Integrating constraints from surface geology and geophysics with mantle structure. *Earth-Science Reviews*, *124*, 148–183. https://doi.org/10.1016/j.earscirev.2013.05.012

Shillington, D. J., Bécel, A., Nedimović, M. R., Kuehn, H., Webb, S. C., Abers, G. A., et al. (2015). Link between plate fabric, hydration and subduction zone seismicity in Alaska. *Nature Geoscience*, *8*(12), 961–964. https://doi.org/10.1038/ngeo2586

Smith, M. L., & Dahlen, F. A. (1973). The azimuthal dependence of love and Rayleigh wave propagation in a slightly anisotropic medium. *Journal of Geophysical Research*, *78*(17), 3321–3333. https://doi.org/10.1029/JB078i017p03321

Snieder, R. (2004). Extracting the Green's function from the correlation of coda waves: A derivation based on stationary phase. *Physical Review E*, *69*(4), 046610. https://doi.org/10.1103/physreve.69.046610

Spica, Z., Perton, M., Calò, M., Legrand, D., Córdoba-Montiel, F., & Iglesias, A. (2016). 3-D shear wave velocity model of Mexico and South US: Bridging seismic networks with ambient noise cross-correlations (C1) and correlation of coda of correlations (C3). *Geophysical Journal International*, *206*(3), 1795–1813. https://doi.org/10.1093/gji/ggw240

Stehly, L., Campillo, M., Froment, B., & Weaver, R. L. (2008). Reconstructing Green's function by correlation of the coda of the correlation (C^3) of ambient seismic noise. (1978–2012). *Journal of Geophysical Research*, *113*(B11), B11306. https://doi.org/10.1029/2008jb005693

Tape, C., & Lomax, A. (2022). Aftershock regions of Aleutian-Alaska megathrust earthquakes, 1938–2021. *Journal of Geophysical Research: Solid Earth*, *127*(7), e2022JB024336. https://doi.org/10.1029/2022jb024336

Tian, Y., & Ritzwoller, M. H. (2017). Improving ambient noise cross-correlations in the noisy ocean bottom environment of the Juan de Fuca plate. *Geophysical Journal International*, *210*(3), 1787–1805. https://doi.org/10.1093/gji/ggx281

Till, A. (2016). Synthesis of Jurassic and Early Cretaceous crustal evolution along the southern margin of the Arctic Alaska–Chukotka microplate and implications for defining tectonic boundaries active during opening of Arctic Ocean basins. *Lithosphere*, *8*(3), 219–237. https://doi.org/10.1130/L471.1

Venereau, C. M. A., Martin-Short, R., Bastow, I. D., Allen, R. M., & Kounoudis, R. (2019). The role of variable slab dip in driving mantle flow at the eastern edge of the Alaskan subduction margin: Insights from shear-wave splitting. *Geochemistry, Geophysics, Geosystems*, *20*(5), 2433–2448. https://doi.org/10.1029/2018gc008170

Wang, Y., & Tape, C. (2014). Seismic velocity structure and anisotropy of the Alaska subduction zone based on surface wave tomography. *Journal of Geophysical Research: Solid Earth*, *119*(12), 8845–8865. https://doi.org/10.1002/2014jb011438

Ward, K. M., & Lin, F. (2018). Lithospheric structure across the Alaskan cordillera from the joint inversion of surface waves and receiver functions. *Journal of Geophysical Research: Solid Earth*, *123*(10), 8780–8797. https://doi.org/10.1029/2018jb015967

Wessel, P., Luis, J. F., Uieda, L., Scharroo, R., Wobbe, F., Smith, W. H. F., & Tian, D. (2019). The generic mapping Tools version 6. *Geochemistry, Geophysics, Geosystems*, *20*(11), 5556–5564. https://doi.org/10.1029/2019GC008515

Xie, J., Ritzwoller, M. H., Brownlee, S. J., & Hacker, B. R. (2015). Inferring the oriented elastic tensor from surface wave observations: Preliminary application across the western United States. *Geophysical Journal International*, *201*(2), 996–1021. https://doi.org/10.1093/gji/ggv054

Xie, J., Ritzwoller, M. H., Shen, W., & Wang, W. (2017). Crustal anisotropy across eastern Tibet and surroundings modeled as a depth-dependent tilted hexagonally symmetric medium. *Geophysical Journal International*, *209*(1), 466–491. https://doi.org/10.1093/gji/ggx004

Xie, J., Ritzwoller, M. H., Shen, W., Yang, Y., Zheng, Y., & Zhou, L. (2013). Crustal radial anisotropy across eastern Tibet and the western Yangtze craton. *Journal of Geophysical Research: Solid Earth*, *118*(8), 4226–4252. https://doi.org/10.1002/jgrb.50296

Yang, X., & Gao, H. (2020). Segmentation of the Aleutian-Alaska subduction zone revealed by full-wave ambient noise tomography: Implications for the along-strike variation of volcanism. *Journal of Geophysical Research: Solid Earth*, *125*(11), e2020JB019677. https://doi.org/10.1029/2020jb019677

Yang, Y., Ritzwoller, M. H., Lin, F.-C., Moschetti, M. P., & Shapiro, N. M. (2008). Structure of the crust and uppermost mantle beneath the western United States revealed by ambient noise and earthquake tomography. (1978–2012). *Journal of Geophysical Research*, *113*(B12), B12310. https://doi.org/10.1029/2008jb005833

Yao, H., Hilst, R. D. V. D., & Hoop, M. V. D. (2006). Surface-wave array tomography in SE Tibet from ambient seismic noise and two-station analysis—I. Phase velocity maps. *Geophysical Journal International*, *166*(2), 732–744. https://doi.org/10.1111/j.1365-246x.2006.03028.x

Zhang, S., Feng, L., & Ritzwoller, M. H. (2020). Three-station interferometry and tomography: Coda versus direct waves. *Geophysical Journal International*, *221*(1), 521–541. https://doi.org/10.1093/gji/ggaa046

Zhang, S., Wang, H., Wu, M., & Ritzwoller, M. H. (2021). Isotropic and azimuthally anisotropic Rayleigh wave dispersion across the Juan de Fuca and Gorda plates and U.S. Cascadia from earthquake data and ambient noise two- and three-station interferometry. *Geophysical Journal International*, *226*(2), 862–883. https://doi.org/10.1093/gji/ggab142

Zhang, Y., Li, A., & Hu, H. (2019). Crustal structure in Alaska from receiver function analysis. *Geophysical Research Letters*, *46*(3), 1284–1292. https://doi.org/10.1029/2018gl081011